Anthropogenic CO_2 monitoring satellite mission: the need for multi-angle polarimetric observations

Stephanie P. Rusli[1], Otto Hasekamp[1], Joost aan de Brugh[1], Guangliang Fu[1], Yasjka Meijer[2], and Jochen Landgraf[1]

[1]SRON Netherlands Institute for Space Research, Sorbonnelaan 2, 3584 CA Utrecht, The Netherlands
[2]European Space Agency, Keplerlaan 1, 2201 AZ Noordwijk, The Netherlands

Abstract. Atmospheric aerosols have been known to be a major source of uncertainties in CO_2 concentrations retrieved from space. In this study, we investigate the added value of multi-angle polarimeter (MAP) measurements in the context of the Copernicus candidate mission for anthropogenic CO_2 monitoring (CO2M). To this end, we compare aerosol-induced XCO_2 errors from standard retrievals using spectrometer only (without MAP) with those from retrievals using both MAP and spectrometer.

5 MAP observations are expected to provide information about aerosols that is useful for improving XCO_2 accuracy. For the purpose of this work, we generate synthetic measurements for different atmospheric and geophysical scenes over land, based on which XCO_2 retrieval errors are assessed. We show that the standard XCO_2 retrieval approach that makes no use of auxiliary aerosol observations returns XCO_2 errors with an overall bias of 1.12 ppm, and a spread (defined as half of the 15.9th to the 84.1th percentile range) of 2.07 ppm. The latter is far higher than the required XCO_2 accuracy (0.5 ppm) and precision (0.7

10 ppm) of the CO2M mission. Moreover, these XCO_2 errors exhibit a significantly larger bias and scatter at high aerosol optical depth, high aerosol altitude, and low solar zenith angle, which could lead to a worse performance in retrieving XCO_2 from polluted areas where CO_2 and aerosols are co-emitted. We proceed to determine MAP instrument specifications in terms of wavelength range, number of viewing angles, and measurement uncertainties that are required to achieve XCO_2 accuracy and precision targets of the mission. Two different MAP instrument concepts are considered in this analysis. We find that for either

15 concept, MAP measurement uncertainties on radiance and degree of linear polarization should be no more than 3% and 0.003, respectively. Adopting the derived MAP requirements, a retrieval exercise using both MAP and spectrometer measurements of the synthetic scenes delivers XCO_2 errors with an overall bias of -0.004 ppm and a spread of 0.54 ppm, implying compliance with the CO2M mission requirements; the very low bias is especially important for proper emission estimates. For the test ensemble, we find effectively no dependence of the XCO_2 errors on aerosol optical depth, altitude of the aerosol layer, and

20 solar zenith angle. These results indicate a major improvement in the retrieved XCO_2 accuracy with respect to the standard retrieval approach, which could lead to a higher data yield, better global coverage, and a more comprehensive determination of CO_2 sinks and sources. As such, this outcome underlines the contribution of, and therefore the need for, a MAP instrument onboard the CO2M mission.

1 Introduction

25   Carbon dioxide is the most important greenhouse gas in our atmosphere. It accounts for 76% of the total anthropogenic green-
house gas emissions in 2010, according to the latest assessment report (2014) of IPCC (Intergovernmental Panel on Climate
Change). In an international effort to mitigate climate change, 195 countries signed the Paris agreement (United Nations Frame-
work Convention on Climate Change, 2015) that aims to limit global temperature rise to less than 2 degrees Celcius above the
pre-industrial levels by reducing greenhouse gas emissions. To achieve this goal, quantifications of CO_2 emissions on a national
30   scale with adequate temporal and spatial resolution, and a global coverage are necessary for the implementation and evaluation
of carbon reduction policies (Ciais et al., 2014). Space-based observations have the capacity to perform such task and will
therefore play an important role in complementing and reinforcing CO_2 inventories (Ciais et al., 2015; Pinty et al., 2017). For
this reason, the European Comission and the European Space Agency (ESA) proposed the Anthropogenic Carbon Dioxide
Monitoring (CO2M) satellite mission as a part of a larger-scale CO_2 initiative within Europe's Earth observation programme
35   Copernicus to monitor and verify man-made CO_2 emissions and their trends (Pinty et al., 2017).

The CO2M mission is designed as a constellation of up to 3 satellites with imaging capabilities and a revisit time of 2-3
days for latitudes (poleward of) 40 degrees. Each satellite carries a primary sounder, that is a nadir-looking spectrometer that
will deliver measurements of column-averaged dry-air mole fraction of carbon dioxide XCO_2 , defined as the ratio of the
total column of CO_2 to that of dry air. As opposed to currently operational CO_2 missions that are designed to observe natural
40   CO_2 fluxes, with the exception of OCO-3 (Basilio et al., 2019), the CO2M mission is intended to measure anthropogenic
emissions (Pinty et al., 2017). With fossil CO_2 emissions primarily concentrated in urban areas, industrial sites, and point
sources such as power plants and refineries, it is important to detect and localize these hotspots. Auxiliary measurements of NO_2
that are co-emitted with CO_2 plumes are proposed to help the mission distinguish anthropogenic from biospheric CO_2 signals
(Kuhlmann et al., 2019). To further resolve and quantify these emissions, Ciais et al. (2015); Crisp et al. (2018) suggest that
45   XCO_2 images should have a spatial resolution of about 4 km^2, an XCO_2 precision ≤ 0.7 ppm, with XCO_2 systematic errors
of 0.5 ppm or less (Meijer et al., 2019). Such XCO_2 accuracy requirement becomes a challenge when aerosols and thin clouds
are not properly taken into account in the retrieval.

Scattering by aerosols and cirrus has long been identified as one of the main sources of uncertainties in retrieving XCO_2 from
solar backscattered radiation (e.g. Kuang et al. (2002); Houweling et al. (2005); Jung et al. (2016)). The presence of aerosols
50   can shorten or enhance the light path, depending on the altitude of the aerosol layer and on the reflection properties of the
underlying surface. In effect, this alters the depth of CO_2 absorption features in that they appear shallower/deeper, which
can be falsely interpreted as lower/higher atmospheric CO_2 concentration. Depending on the observed atmospheric scene and
surface albedo, neglecting scattering in the retrieval can lead to substantial XCO_2 errors, which are often higher than 1%
(about 4 ppm) (Aben et al., 2007; Butz et al., 2009). Methods to correct or compensate for the light path modification typically
55   include explicit parametrization of aerosols and clouds in the XCO_2 retrieval as proxies to the actual scattering (e.g. Kuang
et al. (2002); Oshchepkov et al. (2008); Butz et al. (2011); Morino et al. (2011); Reuter et al. (2017); Nelson and O'Dell
(2019)). This approach usually involves adding one or more types of scattering particles in the forward model and retrieving

their properties while using data limited to radiometric observations. The resulting XCO_2 uncertainties are in most cases still larger than about 1 ppm (e.g. Butz et al. (2009)), which is above the CO2M error requirements.

60 In this paper, we explore the potential of having auxiliary aerosol-dedicated measurements alongside the CO2M spectrometer measurements to help achieve the required XCO_2 accuracy. Here, we utilize the capability of a Multi-Angle Polarimeter (MAP), which measures radiance and degree of linear polarization (DLP) simultaneously at multiple wavelengths and at multiple viewing angles. The proper interpretation of such observations are currently considered the most advanced aerosol remote sensing approach and provide the most comprehensive information about aerosol properties (Dubovik et al., 2019). There is

65 a large variety of orbital MAP instruments, which can be broadly classified into two instrument concepts considered for the CO2M mission, referred to here as MAP-mod and MAP-band concepts. A MAP-mod instrument employs spectral polarization modulation technique such that the polarization information is encoded in the modulation pattern of the radiance spectrum (Snik et al., 2009). On the other hand, a bandpass polarimeter (MAP-band) measures radiance and polarization at specific spectral channels. Most MAP instruments fall into the MAP-band category, including the series of POLDER instruments (De-

70 schamps et al., 1994; Tanré et al., 2011), the future 3MI instrument (Fougnie et al., 2018) on EUMETSAT Polar System - Second Generation, Multi-Angle Imager for Aerosols (MAIA) (Diner et al., 2018), and Hyper-Angular Rainbow Polarimeter-2 (HARP2) (Martins et al., 2018). Linear error analysis to derive the optimal instrument specification for each of the two MAP concepts with regard to wavelength range, number of viewing angles and the measurement uncertainties are a part of our study here. We investigate the added value of a MAP instrument as part of the CO2M mission, by comparing aerosol-induced

75 XCO_2 errors from retrievals using spectrometer data only with the errors from retrievals using the combined spectrometer and MAP measurements. For the retrieval input, we generate synthetic measurements that correspond to an ensemble of atmospheric and geophysical scenes over land. The MAP instrument for which the synthetic measurements are generated, is tailored to the CO2M mission precision and accuracy requirements.

  In the next section, we present the generic instrument description of the spectrometer and the two MAP instrument concepts used in this study. Section 3 details our three approaches to evaluate aerosol-induced XCO_2 errors, i.e. a joint retrieval method

80 that enables a synergistic use of MAP and spectrometer measurements, a linear error analysis which is employed to derive MAP instrument requirements, and a spectrometer-only retrieval method which is applied to a standard XCO_2 retrieval without the auxiliary MAP observations. Section 4 describes the ensemble of 500 scenes for which synthetic measurements are generated; these are used in the retrieval exercises that follow. In Section 5, we perform XCO_2 retrievals using only spectrometer measure-

85 ments and present the results. Section 6 is dedicated to the MAP requirement study in which we apply the linear error analysis to determine the baseline setup for two MAP instrument concepts. In section 7, we adopt one of the baseline MAP setups and implement XCO_2 retrievals assuming both MAP and spectrometer measurements are available. The retrieved XCO_2 are assessed in the same way as in the spectrometer-only approach and the comparison between the resulting XCO_2 uncertainties is discussed here. The final section summarizes the paper.

2 Instruments

For the CO2M mission, a 3-band spectrometer is envisaged to be the main instrument that provides measurements necessary for the XCO_2 retrieval. The 3 bands comprise a NIR band at 765 nm and two shortwave infrared bands at 1.6 μm (SWIR1) and 2.0 μm (SWIR2). The NIR band, as well as the strong CO_2-absorption band in the SWIR2 contain information about aerosols and cirrus. We adopt here the spectrometer spectral properties as proposed for the CO2M mission, given in Table 1. Noise on radiance I is calculated from $\mathrm{SNR} = a_{\mathrm{noise}} I / \sqrt{(a_{\mathrm{noise}} I + b_{\mathrm{noise}})}$, in which a_{noise} and b_{noise} are constants specific to each spectral window. The a_{noise} and b_{noise} values (B. Sierk, private communication) are provided in Table 1 as well.

Table 1. Setup of the CO2M spectrometer

Band ID	spectral range [nm]	spectral resolution [nm]	spectral sampling ratio	a_{noise} [photons^{-1}cm^2 s nm sr]	b_{noise}
NIR	747-773	0.12	3	2.0×10^{-8}	19600
SWIR1	1590-1675	0.30	3	1.32×10^{-7}	202500
SWIR2	1990-2095	0.35	3	1.54×10^{-7}	202500

In our study, we consider two MAP instrument concepts, i.e. MAP-mod and MAP-band. Here, the MAP-mod instrument inherits from the SPEXone instrument (Hasekamp et al., 2019), which will fly on the NASA PACE mission, scheduled to launch in 2022. SPEXone will provide measurements in the visible between 385-770 nm at 5 viewing angles. In the MAP-mod concept, the polarimetric spectral resolution, which derives from the modulation period, becomes coarser at longer wavelengths while the radiance measurements can be obtained at the intrinsic spectral resolution of the instrument (Rietjens et al., 2015). Unlike a MAP-mod instrument that measures a continuous spectrum, a MAP-band instrument measures radiance and polarization at discrete spectral bands. Here, the spectral bands are specified close to the 3MI VNIR channels where both radiance and polarization are measured (Fougnie et al., 2018).

3 Methods

3.1 Joint MAP and spectrometer retrieval

To enable XCO_2 retrievals using MAP and spectrometer measurements in a synergistic way, we developed a joint retrieval algorithm. It is built upon an existing aerosol retrieval algorithm (Hasekamp et al., 2011; Fu and Hasekamp, 2018; Fu et al., 2020) to include features related to trace gas retrieval, with some spectrometer-specific functionalities incorporated in it. The joint retrieval tool can be used with either the MAP-mod or the MAP-band design. Although the algorithm is capable to simultaneously retrieve aerosol properties and the trace gas total columns, in this work we are interested primarily in XCO_2 and do not discuss the retrieved aerosol properties.

In this retrieval, the concept of inverse modeling applies, in which state vector $\mathbf{x}$ is updated until it produces modeled measurements that fit the measurement vector $\mathbf{y}$ well enough. The modeled measurements or forward model $\mathbf{F}$ relates the state

115 and measurement vectors via

$$\mathbf{y} = \mathbf{F}(\mathbf{x}, \mathbf{b}) + \epsilon_{\mathbf{y}} + \epsilon_{\mathbf{F}}, \tag{1}$$

where the terms $\epsilon_{\mathbf{y}}$ and $\epsilon_{\mathbf{F}}$ represent the measurement error and forward model error, while $\mathbf{b}$ constitutes auxiliary parameters needed to compute the forward model but are not retrieved. The $\mathbf{y}$ vector consists of the MAP and spectrometer measurements.

3.1.1 Forward model

120 The forward model computes the Stokes vector, which describes the radiance and polarization state of light, at a certain wavelength and at a certain viewing angle for a specific atmospheric and geophysical scene. Degree of linear polarization (DLP) is then derived from the first three components of the vector I, Q, U, i.e. $\text{DLP} = \sqrt{Q^2 + U^2}/I$, where I constitutes the radiance. We consider both aerosols and trace gases in the model atmosphere. First, optical properties of molecules and aerosols are calculated. Aerosol optical properties are derived from the microphysical properties using tabulated kernels for a

125 mixture of spheroids and spheres (Dubovik et al., 2006). The complex refractive index of aerosols is computed as a function of MAP wavelengths, but is assumed constant with wavelength inside a spectrometer window. Optical thickness due to molecular scattering is determined from the Rayleigh scattering cross section (Bucholtz, 1995). In the three spectrometer windows, molecular absorption features correspond to O_2 in the NIR band, H_2O, CO_2 in the two SWIR bands, and CH_4 in the SWIR1 band. Molecular absorption optical thickness is computed from the absorption cross-section values, which are pre-calculated

130 from the latest spectroscopic databases (Tran et al., 2006; Rothman et al., 2009; Scheepmaker et al., 2013) and stored in a look-up table as a function of pressure, temperature and wavenumber.

Stokes parameters are computed from the optical properties via the radiative transfer model based on the work of Landgraf et al. (2001); Hasekamp and Landgraf (2002); Hasekamp and Landgraf (2005). For the polarimeter, Stokes parameters are calculated at each MAP wavelength. These modeled radiances and DLP directly represent the simulated MAP observations.

135 To create spetrometer synthetic observations, optical thickness due to molecular and aerosol scattering and absorption and the radiance spectra are computed on a finely-sampled wavelength grid within each spectrometer window. Multiple scattering contribution to the radiances is approximated by the linear-k approach (Hasekamp and Butz, 2008) to reduce computational time. The measured radiances are simulated by convolving the modeled radiances on the fine spectral grid with the instrument spectral response function, with random noise added afterwards. The instrument response function is modeled as a Gaussian

140 with a Full Width at Half Maximum set to the spectral resolution listed in Table 1 and the noise follows the SNR defined in section 2.

The model atmosphere consists of 15 predefined height layers. Atmospheric vertical profiles of temperature, H_2O, CO_2, and CH_4 are provided as input. Aerosols consist of two modes, referred to as the fine and the coarse mode. The size distribution of each mode is quantified by a lognormal distribution (see Appendix A). To describe the vertical distribution of aerosols in the

145 atmosphere, we adopt a Gaussian shape such that the number density of each aerosol mode at layer k is given by

$$N_{0,k} = N_{\mathrm{aer}} h(z_k) \Delta z_k, \tag{2}$$

where

$$h(z_k) = A \exp\left(-\frac{4(z_k - z_{\mathrm{aer}})^2 \ln 2}{w_{\mathrm{aer}}^2}\right). \tag{3}$$

N_{aer} is the vertically integrated column number density, A is a normalization constant, z_k is the height of layer k, w_{aer} is the

150 width of the aerosol height distribution and z_{aer} is the aerosol mean height (Butz et al., 2009, 2010).

The refractive index of each aerosol mode is defined by a linear combination of two aerosol types, such that the complex refractive index of a mode as a function of wavelength becomes

$$m(\lambda) = \sum_{l=1}^{2} c_l m_l(\lambda) \tag{4}$$

with $0.0 \leq c_l \leq 1.0$. $m_l(\lambda)$ is a wavelength-dependent complex refractive index for a certain aerosol type l, i.e. dust, inorganic

155 matter (inorg), or black carbon (BC). The model size distribution and composition per mode do not vary with height. The aerosol particles are assumed to be a mixture of spheroids and spheres, where the proportion of the latter is characterized by the fraction of spheres (f_{sphere}).

To account for the reflection and polarization properties of the surface, the retrieval algorithm employs semi empirical bidirectional reflectance distribution function (BRDF) and bidirectional polarization distribution function (BPDF) models. The

160 BRDF is characterized by the surface total reflectances R_I that are modeled using a linear combination of kernels in the form

$$R_I(\lambda, \theta_\nu, \theta_0, \Delta\phi) = k_\lambda[1 + k_{\mathrm{geo}} f_{\mathrm{geo}}(\theta_\nu, \theta_0, \Delta\phi) + k_{\mathrm{vol}} f_{\mathrm{vol}}(\theta_\nu, \theta_0, \Delta\phi)] \tag{5}$$

(Litvinov et al., 2011), where θ_ν, θ_0 are the viewing and solar zenith angles, and $\Delta\phi$ is the relative azimuth angle. We use the Ross-thick kernel for volumetric scattering kernel f_{vol}, and the Li-sparse kernel as geometric-optical scattering kernel f_{geo} (Wanner et al., 1995). The BPDF is modeled according to the linear one-parameter model proposed by Maignan et al. (2009),

165 with α being the only free parameter.

3.1.2 State vector

Although our main focus in this retrieval is XCO$_2$, we also retrieve aerosol properties, together with surface attributes, and the total columns of CH$_4$ and H$_2$O. We take the input vertical profiles of the trace gases as a given and retrieve the total columns via scaling factors. Here, the prior and first guess of the scaling factor for each gas species are always 1.0, corresponding to the

170 input total column. The majority of aerosol properties are included in the state vector; there are only 4 aerosol parameters that are not retrieved, i.e. f_{sphere}, z_{aer} of the fine-mode aerosol, and w_{aer} for both modes. In our retrievals with synthetic data here, the four parameters are fixed to the true values. Regarding the surface attributes, k_λ at every measured MAP wavelength and for every spectrometer window, $k_{\mathrm{vol}}, k_{\mathrm{geo}}$, and α are considered the unknowns and therefore are part of the state vector. The complete list of the state variables, along with the prior values and prior uncertainties, is given in Table 2.

Table 2. State variables in the joint retrieval

	State parameter	Prior	Prior error
	XCO_2 scaling factor	1.0	1.0
trace gas	H_2O scaling factor	1.0	1.0
	CH_4 scaling factor	1.0	1.0
	r_{eff} [μm]	0.2	0.1
fine-mode	v_{eff}	0.2	0.05
aerosol	c_1 (inorg)	0.9	0.1
	c_2 (BC)	0.1	0.1
	τ at 550 nm	0.2	1.0
	r_{eff} [μm]	1.5	1.0
	v_{eff}	0.6	0.1
coarse-mode	c_1 (dust)	0.5	0.1
aerosol	c_2 (inorg)	0.5	0.1
	τ at 550 nm	0.05	0.2
	f_{sphere}	0.05	0.5
	z_{aer} [m]	6500	4000
	k_{geo}	0.0	0.25
surface	k_{vol}	0.0	1.0
properties	multiple k_λ	0.0	0.5
	α	1.0	2.0

3.1.3 Inversion procedure

The goal of the retrieval is to find $\mathbf{x}$ which would result in $\mathbf{F}(\mathbf{x}, \mathbf{b})$ that best matches $\mathbf{y}$. This is achieved by minimizing the cost function

$$\hat{\mathbf{x}} = \underset{\mathbf{x}}{\arg\min} \left(\|\mathbf{S_y}^{-\frac{1}{2}}(\mathbf{y} - \mathbf{F}(\mathbf{x}, \mathbf{b}))\|^2 + \gamma^2 \|\mathbf{W}(\mathbf{x} - \mathbf{x_a})\|^2 \right) \tag{6}$$

$\mathbf{x_a}$ is the prior state vector, $\mathbf{W}$ is a weight matrix, while γ is the Phillips-Tikhonov regularization parameter (Phillips, 1962; Tikhonov, 1963). Regularization is needed to obtain a stable solution since the inverse problem is ill-posed. The weight matrix $\mathbf{W}$ is constructed in such a way that it brings all state vector elements to the same order of magnitude; it is also used in the inversion to give more freedom to some state vector parameters, for which the prior information is assumed less reliable compared to the others. Here, $\mathbf{W} = \mathbf{S_a}^{-\frac{1}{2}}$ such that for $\gamma = 1$, Eq. (6) reduces to the Optimal Estimation cost function.

Due to the non-linearity of the forward model, the minimization problem is solved in an iterative manner. At every iteration step, $\mathbf{F}(\mathbf{x})$ is linearized such that at iteration n:

$$\mathbf{F}(\mathbf{x}_{n+1}, \mathbf{b}) \approx \mathbf{F}(\mathbf{x}_n, \mathbf{b}) + \mathbf{K}(\mathbf{x}_{n+1} - \mathbf{x}_n). \tag{7}$$

$\mathbf{K}$ is the Jacobian matrix containing partial derivatives of forward model element F_i with respect to state variable x_j, i.e.

$$K_{ij} = \frac{\partial F_i(\mathbf{x}_n)}{\partial x_j}. \tag{8}$$

The linearization in Eq. (7) modifies the optimization problem to

$$\tilde{\mathbf{x}}_{n+1} = \arg\min_{\mathbf{x}} \left(\|\tilde{\mathbf{y}} + \tilde{\mathbf{K}}\tilde{\mathbf{x}}_n - \tilde{\mathbf{K}}\tilde{\mathbf{x}}\|^2 + \gamma^2 \|\tilde{\mathbf{x}} - \tilde{\mathbf{x}}_{\mathbf{a}}\|^2 \right), \tag{9}$$

with

$$\tilde{\mathbf{x}} = \mathbf{W}\mathbf{x}, \tag{10}$$

$$\tilde{\mathbf{y}} = \mathbf{S_y}^{-\frac{1}{2}}(\mathbf{y} - \mathbf{F}(\mathbf{x}_n)), \tag{11}$$

$$\tilde{\mathbf{K}} = \mathbf{S_y}^{-\frac{1}{2}}\mathbf{K}\mathbf{W}^{-1}. \tag{12}$$

The solution is found using an iterative Gauss-Newton method and expressed in terms of the departure $\Delta\tilde{\mathbf{x}}$ from $\tilde{\mathbf{x}}_n$ (Rodgers, 2000). Given that the forward model is highly non linear, the retrieval could diverge when the current $\tilde{\mathbf{x}}_n$ is far from the solution. To avoid that, we reduce the step size $\Delta\tilde{\mathbf{x}}$ by applying the Λ factor, i.e.

$$\tilde{\mathbf{x}}_{n+1} = \tilde{\mathbf{x}}_n + \Lambda(\Delta\tilde{\mathbf{x}}), \tag{13}$$

with

$$\Delta\tilde{\mathbf{x}} = (\tilde{\mathbf{K}}^T\tilde{\mathbf{K}} + \gamma^2\mathbf{I})^{-1}[\tilde{\mathbf{K}}^T\tilde{\mathbf{y}} - \gamma^2(\tilde{\mathbf{x}}_n - \tilde{\mathbf{x}}_{\mathbf{a}})] \tag{14}$$

At each iteration step, we compute a fast and simplified forward model using a combination of 5 possible γ and 10 possible Λ values. γ is varied from 0.1 to 5 whereas Λ is varied from 0.1 and 1.0. The combination of γ and Λ that delivers the best match to the measurements, via χ^2 assessment, is adopted in Eq. (14) to compute the step size. The iteration in the inversion starts with a first guess $\tilde{\mathbf{x}}_1$ that is generated via a look-up table retrieval.

3.2 Linear error analysis

Linear error analysis allows XCO_2 errors to be derived in a way that mimics as close as possible an iterative retrieval method and so is particularly useful in performing the MAP requirement study. Linear error analysis delivers an aerosol-induced XCO_2 error $\langle \Delta XCO_2 \rangle$ that is representative in the statistical sense. It is impractical to derive this error using iterative retrieval method, given the large number of scenarios and instrument setups that we evaluate in the requirement study. The basic principles of the error analysis that we employ can be found in Rodgers (2000). Here we describe the mathematical formalism of the analysis.

In order to estimate $\langle \Delta XCO_2 \rangle$, the error analysis follows a two-step approach. The first step (step 1) corresponds to the aerosol retrieval using MAP. Here the uncertainties on aerosol parameters are derived. The second step (step 2) represents XCO_2 retrieval using spectrometer measurements where the aerosol uncertainties from step 1 are propagated to result in

$\langle \Delta XCO_2 \rangle$. In both steps, aerosols are parametrized in the same way as in the section 3.1.1. As in section 3.1.2, we do not retrieve w_{aer} of both modes, z_{aer} and f_{sphere} of the fine mode, which leaves us with 12 aerosol parameters in the state vector.

215

We compute for each scenario two Jacobian matrices. One of the Jacobians is associated to retrieval step 1 with a given MAP setup ($\mathbf{K}_{\mathrm{MAP}}$), and the other belongs to retrieval step 2 ($\mathbf{K}_{\mathrm{spc}}$). State variables in step 1 comprise aerosol and surface

220 parameters (see section 3.1.1 for details). Measurement variables of step 1 consist of radiances and DLP; their composition depends on the MAP instrument setup being used. State vector of retrieval step 2 follows that used in the spectrometer-only retrieval described in section 3.3, with the exception of the aerosol parameters, i.e. here we use the bimodal lognormal model (Eq. A1) and fit 12 parameters (Table 2). Both $\mathbf{K}_{\mathrm{spc}}$ and $\mathbf{K}_{\mathrm{MAP}}$ are calculated at the true state vector values and each of them contains derivatives of the corresponding measurements with respect to 12 aerosol parameters.

225 Errors on the retrieved aerosol properties from step 1 comprise the smoothing errors and the MAP-measurement-noise-induced error (retrieval noise). The smoothing error is formulated as

$$\mathbf{S}_{\mathrm{MAP}}^{\mathrm{sm}} = (\mathbf{G}_{\mathrm{MAP}}\mathbf{K}_{\mathrm{MAP}} - \mathbf{I})\mathbf{S}_{\mathrm{a,MAP}}(\mathbf{G}_{\mathrm{MAP}}\mathbf{K}_{\mathrm{MAP}} - \mathbf{I})^{T}, \tag{15}$$

whereas the retrieval noise reads

$$\mathbf{S}_{\mathrm{MAP}}^{\mathrm{ns}} = \mathbf{G}_{\mathrm{MAP}}\mathbf{S}_{\mathrm{y,MAP}}\mathbf{G}_{\mathrm{MAP}}^{T}. \tag{16}$$

230 $\mathbf{S}_{\mathrm{a,MAP}}$ is a MAP prior error covariance matrix, which is a diagonal matrix containing squared prior errors. The values of prior errors that we use here for the aerosol and surface variables are the same as those stated in Table 2. $\mathbf{S}_{\mathrm{y,MAP}}$ is a measurement error covariance matrix containing squared values of MAP measurement errors along the diagonal axis. The individual radiometric and polarimetric measurements are assumed uncorrelated, so the off-diagonal elements are set to zero. $\mathbf{G}_{\mathrm{MAP}}$ is the gain matrix that relates the MAP measurement errors with the noise in MAP state parameters and it follows that

235 $$\mathbf{G}_{\mathrm{MAP}} = (\mathbf{K}_{\mathrm{MAP}}^{T}\mathbf{S}_{\mathrm{y,MAP}}^{-1}\mathbf{K}_{\mathrm{MAP}} + \mathbf{S}_{\mathrm{a,MAP}}^{-1})^{-1}\mathbf{K}_{\mathrm{MAP}}^{T}\mathbf{S}_{\mathrm{y,MAP}}^{-1}. \tag{17}$$

The total aerosol (posterior) error covariance matrix is then

$$\mathbf{S}_{\mathrm{MAP}}^{\mathrm{tot}} = \mathbf{S}_{\mathrm{MAP}}^{\mathrm{ns}} + \mathbf{S}_{\mathrm{MAP}}^{\mathrm{sm}}. \tag{18}$$

Cropping $\mathbf{S}_{\mathrm{MAP}}^{\mathrm{tot}}$ to keep only variances and covariances of the 12 aerosol parameters (i.e. excluding the surface parameters) results in $\mathbf{S}_{\mathrm{aer}}^{\mathrm{tot}} \in \mathbb{R}^{12 \times 12}$.

240 The matrix $\mathbf{S}_{\mathrm{aer}}^{\mathrm{tot}}$, which represents the total uncertainties in aerosol parameters retrieved from MAP measurements, is then passed on to the second part of the error analysis. At this stage, the aerosol errors are mapped into spectrometer measurement errors using $\mathbf{K}_{\mathrm{spc}}$. The spectrometer measurement errors are in turn propagated into the errors of the step-2 state variables using the spectrometer gain matrix $\mathbf{G}_{\mathrm{spc}}$. The mathematical expression for this propagation chain in step 2 is

$$\mathbf{S}_{\mathrm{spc}}^{\mathrm{aer}} = \mathbf{G}_{\mathrm{spc}}\,\mathbf{K}_{\mathrm{spc}}^{\mathrm{aer}}\,\mathbf{S}_{\mathrm{aer}}^{\mathrm{tot}}\,(\mathbf{K}_{\mathrm{spc}}^{\mathrm{aer}})^{T}\,\mathbf{G}_{\mathrm{spc}}^{T}, \tag{19}$$

245   where

$$\mathbf{G}_{\mathrm{spc}} = (\mathbf{K}_{\mathrm{spc}}^{T}\mathbf{S}_{\mathrm{y,spc}}^{-1}\mathbf{K}_{\mathrm{spc}} + \gamma^{2}\mathbf{W})^{-1}\mathbf{K}_{\mathrm{spc}}^{T}\mathbf{S}_{\mathrm{y,spc}}^{-1}. \tag{20}$$

$\mathbf{K}_{\mathrm{spc}}^{\mathrm{aer}}$ is a subset of $\mathbf{K}_{\mathrm{spc}}$ containing derivatives with respect to aerosol properties only. The regularization term $\gamma^{2}\mathbf{W}$ is adjusted accordingly to arrive at the typical degrees of freedom between 2 and 3 for aerosol parameters (Guerlet et al., 2013; Wu et al., 2019). $\mathbf{S}_{\mathrm{y,spc}}^{-1}$ is a diagonal matrix containing the squared values of the spectrometer measurement noise.

250   Finally, $\langle\Delta\mathrm{XCO_2}\rangle$ is obtained from

$$\langle\Delta\mathrm{XCO_2}\rangle = \sqrt{\mathbf{S}_{\mathrm{spc}}^{\mathrm{aer}}[1,1]}, \tag{21}$$

where the first diagonal element $\mathbf{S}_{\mathrm{spc}}^{\mathrm{aer}}[1,1]$ is the variance of the CO_2 total column. Note that $\langle\Delta\mathrm{XCO_2}\rangle$ includes the error contribution from the MAP noise, but not from the spectrometer noise.

3.3   Spectrometer-only retrieval

255   To perform XCO_2 retrievals using spectrometer measurements only, we employ the RemoTeC algorithm which was designed for greenhouse gas retrievals using satellite observations (Butz et al., 2009, 2010). The forward modelling adopts the latest version developed for TROPOMI (Hu et al., 2016) and the inversion procedure largely follows Butz et al. (2012). In what follows, we highlight aspects that are specific to this work.

As in the joint retrieval, we retrieve the total column of CO_2 , along with the total columns of two other trace gases i.e. H_2O

260   and CH_4, via scaling factors. Prior values of the total columns are derived from the input profiles, i.e. corresponding to scaling factors of 1. The input profiles of temperature, pressure and the gases are the same as those used in the joint retrieval.

With only spectrometer data available, we resort to a simplifed approximation of aerosols in the retrieval. In the forward model, aerosols are described by a simple model where the size distribution is parametrized by a monomodal power-law function. The power-law distribution is prescribed in Mishchenko et al. (1999) and it reads:

265    $$n(r) = \begin{cases} B, & \text{if } r < r_1. \\ B(r/r_1)^{-\beta}, & \text{if } r_1 < r \le r_2. \\ 0, & \text{if } > r_2. \end{cases} \tag{22}$$

B is the normalization constant and r is the aerosol particle radius. r_1 is fixed to 0.1 μm and r_2 to 10 μm. The height distribution follows Equations (2) and (3) with w_{aer} set to 2 km. The real and imaginary refractive indices are kept constant at 1.4 and -0.003, respectively, in all three spectral windows. Aerosol properties that are retrieved include the optical depth τ at 765 nm (prior=0.1), the size distribution parameter β (prior=4.0), and the mean height z_{aer} (prior=3000 m). This simplified aerosol

270   model is adopted by e.g. Butz et al. (2009); Butz et al. (2012); Hu et al. (2016); Wu et al. (2019, 2020) as the standard approach to account for aerosol effects on the retrieved XCO_2 and XCH_4.

The reflection at the Earth surface is assumed to be Lambertian. Surface reflectance is included in the state vector via the albedo and its wavelength dependence in each window, which are modelled as a first-order polynomial. The prior for the albedo

is the Lambertian-equivalent albedo corresponding to the maximum radiance measured in the retrieval window in question.

275 The slope of the polynomial (wavelength dependence of the albedo) is given a prior of 0.0. Additionally, for each spectral window a spectral shift parameter is retrieved with a prior of 0.0. In total, the state vector consists of 15 variables, i.e. the total columns of three trace gases (CO_2, CH_4, H_2O), 3 aerosol properties, and for each spectral window 2 albedo parameters and 1 spectral shift parameter.

4   Ensemble of synthetic scenes

280 We construct an ensemble of 500 synthetic scenes, characterized by different combinations of trace gas and aerosol content, surface albedo, and solar zenith angle (SZA). Every scene is generated by randomly varying those atmospheric and geophysical properties. The random value is drawn from a uniform distribution within a specific interval.

Given the spectral windows of the CO2M spectrometer, the radiance spectra include absorption features due to CO_2, H_2O, and CH_4. In this ensemble, the vertical profile of the individual gas is fixed and we vary the total column, which is represented

285 by the scaling factor. The scaling factors of CO_2, H_2O, and CH_4 are varied by 5%, 3%, and 6%, corresponding to the intervals [0.95,1.05], [0.97,1.03], and [0.94,1.06], respectively. A scaling factor of 1.0 means that the total column is obtained from vertically integrating the column number density given in the atmospheric input profile, which for CO_2 amounts to 400 ppm. Given that the scaling factors in the scenes are randomized, the true total columns are by intention different from the prior values in our retrieval exercises.

290 Aerosols in every scene are constructed to consist of the fine and the coarse mode. The size distribution of each mode is quantified by a lognormal distribution (Eq. A1). The vertical distribution of an aerosol mode in the atmosphere follows a Gaussian shape (Eq. 3). The refractive index of each aerosol mode is defined by Eq. (4) where the coarse mode is composed of the dust and inorganic types, while the fine mode is made up of inorganic matter and black carbon. The fine mode is set up to consist entirely of spheres, i.e. fraction of spheres $f_{\mathrm{sphere}} = 1.0$, for which the Mie theory applies. The coarse-mode

295 particles are described by a mixture of spheroids and spheres, following Dubovik et al. (2006). Aerosol size distribution and composition of each mode are constant with height. Most of the aerosol parameters are varied randomly, while a few are held fixed. Table 3 provides the complete list of the aerosol properties and the corresponding intervals from which random values are drawn, or the corresponding values for the fixed parameters.

Solar zenith angle is allowed to take any value between 10 and 70 degrees. Surface albedo ρ is determined from the combi-

300 nation of albedos of two surface types, i.e. soil and vegetation. More specifically,

$$\rho = f\rho_{\mathrm{soil}} + (1 - f)\rho_{\mathrm{veg}}, \tag{23}$$

in which ρ_{soil} and ρ_{veg} are provided in a tabular form as a function of wavelength, and f is varied between 0 and 1.

The simulated spectra for the spectrometer-only retrieval (sections 3.3 and 5) are not identical to the simulated spectrometer measurements for the joint retrieval (sections 3.1 and 7). This is because the surface descriptions used in the two retrieval

305 approaches differ. To isolate aerosol-induced errors, we use the same surface model in the forward simulation as in the retrieval.

Table 3. Aerosol properties in the ensemble. The numbers in square brackets specify the interval from which a random value is drawn, whereas a single number indicates a fixed value.

Aerosol parameters	fine mode	coarse mode
r_{eff} [μm]	[0.1,0.3]	[0.65,3.4]
v_{eff}	[0.1,0.3]	[0.45,0.65]
c_1	[0.887,0.975] (inorg)	[0.439,0.512] (dust)
c_2	[0.0,0.05] (BC)	[0.439,0.512] (inorg)
τ at 765 nm	[0.002,0.52]	[0.0048,0.32]
f_{sphere}	1.0	[0.0,0.5]
z_{aer} [m]	1000	[1000,8500]
w_{aer} [m]	2000	2000

Consequently, we use the Lambertian surface assumption to generate spectra for the spectrometer-only retrieval, where ρ at 765, 1600, and 2000 nm are assigned as the albedo in NIR, SWIR1 and SWIR2 windows, respectively. Albedo within a spectral window is not wavelength dependent. For the joint retrieval exercise, synthetic spectra of both the polarimeter and the spectrometer are generated by employing the BRDF and BPDF models (Eq. 5, section 3.1.1), with $k_{\mathrm{vol}} = 1.0$, $k_{\mathrm{geo}} = 0.1$, and

310 $\alpha = 1.0$ (non-Lambertian surface). The values of k_λ are set to ρ at 765, 1600, and 2000 nm for the three spectral windows (k_λ is fixed within a spectrometer window) and to ρ at each MAP wavelength.

Finally, we add random realizations of the instrument noise to the simulated measurements. It is this noisy spectra that are given as input data for the retrievals. For the spectrometer, the noise follows the formulation in section 2. For MAP, the noise on radiance is typically a few percent, while the noise on DLP is of the order of 10^{-3} (the determination of the appropriate

315 noise level is a part of the requirement study in section 6).

5   XCO$_2$ retrieval using CO2M spectrometer measurements only

Here we present the results of RemoTeC iterative retrievals (section 3.3) of XCO$_2$ on 500 synthetic scenes described in section 4, using only spectrometer observations (section 2). The goodness-of-fit of the retrieval results is evaluated via $\chi^2 = \frac{1}{N_{\mathrm{meas}}} \sum_{i=1}^{N_{\mathrm{meas}}} \left(\frac{y_i - F_i}{e_i} \right)^2$. N_{meas} is the total number of measurements, y_i, F_i, e_i represent the (synthetic) measurements, the

320 forward model, and the measurement uncertainties, respectively. Since we use noisy synthetic measurements, we expect that a successful and converged retrieval would have a χ^2 of around 1. Here, we impose a χ^2 criterion by applying a threshold of 1.5. Only for converged retrievals with $\chi^2 \leq 1.5$ do we assess the retrieval error ΔXCO$_2$ and how it depends on some aerosol, surface properties and SZA. ΔXCO$_2$ is the residual XCO$_2$, i.e the retrieved minus the true total column, so it represents the combined effect of aerosol-induced and spectrometer-noise-induced errors on the retrieved XCO$_2$.

325 Out of 500 retrievals, 343 converge and meet the χ^2 criterion (convergence rate of 69%). Figure 1 plots ΔXCO$_2$ of the 343 retrievals as a function of true aerosol optical depth, aerosol height, SZA, and albedo. ΔXCO$_2$ is evidently sensitive to
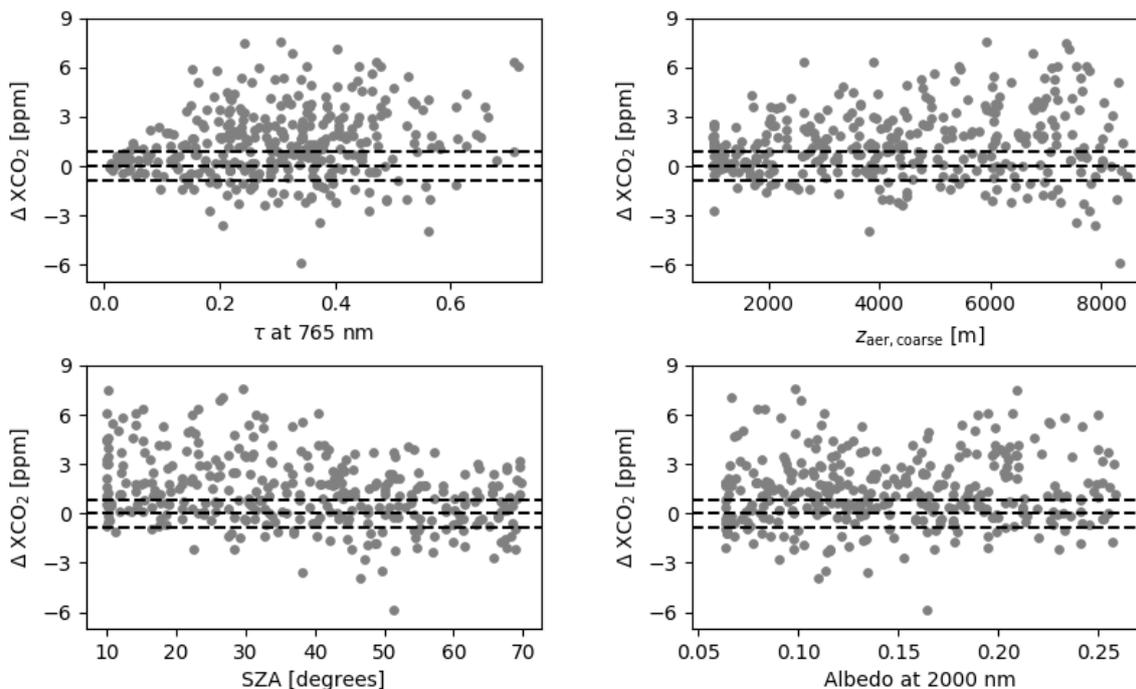
Figure 1. Residual XCO_2 from the converged retrievals using spectrometer measurements only, shown as a function of total aerosol optical depth τ, coarse-mode aerosol height, SZA, and albedo. The input spectra are generated according to the ensemble of synthetic scenes (Section 4). The three dashed horizontal lines indicate ΔXCO_2 at -0.86, 0, and 0.86 ppm.

the changes in aerosol optical depth, aerosol height and the SZA. In what follows, we use the median value of ΔXCO_2 to describe the bias. For $\tau < 0.07$, ΔXCO_2 are relatively unbiased and confined to within ± 1.5ppm. Starting $\tau \sim 0.1$, the scatter in ΔXCO_2 becomes much larger with an overall bias of ~ 1.9 ppm at $\tau \sim 0.5$. Beyond τ of 0.6, there are notably fewer

330 converged retrievals; almost all of them have positive ΔXCO_2. Like the optical depth, aerosol height is fitted in the retrieval. For scenes with a true coarse-mode aerosol height up to 1700 m, ΔXCO_2 is found between -2.7 and +2.6 ppm with a relatively small positive bias of 0.3 ppm. However, as the true coarse-mode aerosol height increases, so do the scatter and the bias in XCO_2. At heights > 7000 m, ΔXCO_2 is distributed between -5.9 and +7.5 ppm with a bias of 1.1 ppm. An opposite trend is seen for SZA where the highest bias is observed for the lowest SZA between 10° and 30°. There, the median value of ΔXCO_2 is

335 1.7 ppm. Between SZA of 60° and 70°, the retrieval bias is the smallest at 0.6 ppm. ΔXCO_2 scatter shows a slight reduction with increasing SZA. Dependency of ΔXCO_2 on the surface albedo at 2000 nm is not apparent in our ensemble; there is a an overall positive bias without any noteworthy correlation. The same can be said about the behaviour of ΔXCO_2 with respect to albedo in the other two spectral windows and about the behaviour of ΔXCO_2 as a function of blended albedo (following the definition in Wunch et al. (2011)).

340   The trends of ΔXCO_2 that we see here are largely consistent with those in Butz et al. (2009). In their 3-band noise-free retrieval exercise, they observed a positive bias in the residual XCO_2 error distribution, that the scatter in XCO_2 errors increased

with aerosol optical thickness, and that the XCO_2 errors did not show a pronounced dependence on surface albedo. For most of the cases with $\tau \leq 0.5$, their XCO_2 errors were confined to less than 1%. Our results reflect all of those findings. Butz et al. evaluated their ensemble at two SZA values, i.e. 30° and 60°, and they found that a positive bias in samples with SZA=60° was

345 stronger than for samples with SZA=30°. This may seem to contradict our result that shows a diminishing positive bias with increasing SZA, but one should note the use of different statistical samplings in our and their analyses, which prevents a direct comparison.

To minimize outlier effects on the statistics, we choose to evaluate the bias and the spread of the ΔXCO_2 distribution using percentiles. We adopt the median (the 50th percentile) as a measure of the bias and $P_{SD} = 0.5 \times (P(84.1) - P(15.9))$ as a

350 measure of the spread, where P(15.9) and P(84.1) are the 15.9th and the 84.1th percentiles. For a normal distribution, P_{SD} reduces to the standard deviation, within which ∼68% of the instances fall. From the 343 retrievals, the median ΔXCO_2 is found at 1.12 ppm and P_{SD} is equal to 2.07 ppm. Our median value is in between the 3-band retrievals of Butz et al. (2009) for SZA=30° (0.42 ppm) and SZA=60° (1.2 ppm), while our P_{SD} is above the standard deviation found by Butz et al. (1.29 for SZA=30° and 1.42 ppm for SZA=60°). Our higher P_{SD} could be attributed, at least partially, to the additional instrument noise

355 in the simulated measurements since Butz et al. used synthetic measurements without noise.

As mentioned above, the accuracy and precision requirements of the CO2M mission are 0.5 and 0.7 ppm, respectively. The quadratic sum amounts to a total XCO_2 uncertainty of 0.86 ppm. With a P_{SD} above 2 ppm, XCO_2 retrievals based on only spectrometer measurements do not meet the mission requirements by a very wide margin (note that we do not apply post-retrieval filtering here). In section 7, we investigate the improvement in XCO_2 accuracy and precision when a MAP instrument

360 is flown aboard the CO2M satellite.

6 MAP requirement analysis

Before we can assess the contribution of a MAP instrument in improving the XCO_2 retrieval performance, we first determine the required specifications for such an instrument given the precision and accuracy threshold of the CO2M mission. As stated in section 2, two alternative MAP instrument concepts are being considered, i.e. MAP-mod and MAP-band. For

365 each concept, we look into multiple instrument configurations to search for the optimal one that meets the CO2M mission requirement by performing linear error analyses (section 3.2). A linear error analysis delivers $\langle \Delta XCO_2 \rangle$ that represents aerosol-induced XCO_2 errors, which consist of both systematic and random components. The MAP instrument noise is included in $\langle \Delta XCO_2 \rangle$ but the spectrometer noise is not accounted for. For a total error budget of 0.86 ppm (quadratic sum of the CO2M accuracy and precision requirements), here we assume equal error contributions from the MAP and from the spectrometer. This

370 means we allocate 0.6 ppm for $\langle \Delta XCO_2 \rangle$ and leave 0.6 ppm for other error sources, e.g. spectrometer noise (the quadratic sum of 0.6 ppm and 0.6 ppm is 0.85 ppm).

We evaluate the performance of MAP instrument setups with respect to three aspects, i.e. radiance and polarization measurement uncertainties, number of viewing angles and the wavelength range. For this purpose, the linear error analysis is applied to a generic set of study scenarios involving a variety of aerosol and surface properties. Below, we define the study cases,

375 followed by the requirement analysis for the MAP-mod concept, which results in the MAP-mod baseline setup. Afterwards, we present the baseline setup for the MAP-band concept that we determine through a separate error analysis similar to that for the MAP-mod.

6.1 Study cases

We introduce three aerosol cases that form the basis of the scenarios used to derive the requirements. They are referred to as
380 'case 1', 'case 2', and 'case 3'. In all cases, the aerosols are modeled according to the bimodal lognormal size distribution, Gaussian height distribution, and the linear superposition of complex refractive index (Equations A1, 2-4), i.e. the same as the parametrizations used to build the ensemble of synthetic scenes (section 4). The fine mode aerosol is always located at 1 km height in all cases. Case 1 is designed to mimic boundary layer aerosols where the fine and coarse mode aerosols coincide at 1 km. In case 2, the coarse mode represents an elevated layer at 8 km. Case 3 is a mid-troposphere case where the coarse mode
385 is located at 4 km. All fine mode particles are spherical and non-absorbing, whereas the coarse mode constitute dust particles with $f_{\mathrm{sphere}} = 0.05$. To account for the effects of aerosol load on XCO_2 retrieval, the aerosol optical depth τ of either the fine or the coarse mode is varied to 5 different values in each case. The summary of the aerosol properties for each case is given in Table 4.

Table 4. Aerosol properties adopted in the study cases

Aerosol parameters	Case1		Case 2 / 3	
	fine mode	coarse mode	fine mode	coarse mode
r_{eff} [μm]	0.12	1.6	0.12 / 0.2	1.6
v_{eff}	0.2	0.6	0.2	0.6
f_{sphere}	1.0	0.05	1.0	0.05
c_1	1.0(inorg)	1.0(dust)	1.0(inorg)	1.0(dust)
c_2	0.0(BC)	0.0(inorg)	0.0(BC)	0.0(inorg)
z_{aer} [m]	1000	1000	1000	8000 / 4000
w_{aer} [m]	2000	2000	2000	2000
	0.05,0.1			0.02,0.04
τ at 765 nm	0.15,0.25	0.02	0.2	0.06,0.10,
	0.5			0.15

We consider two types of land surface, i.e. soil and vegetation. These are the basic surface types used to create the 500 syn-
390 thetic scenes (section 4). Albedo values at 765 nm, 1600 nm, 2000 nm for the soil are 0.139,0.298,0.259, and for the vegetation type 0.450,0.230,0.063. We perform the error analysis for two solar zenith angles 30°and 60°. In total, the combination of 2 surface types, 2 SZA values and 15 aerosol variations results in 60 scenarios.

6.2 MAP-mod instrument

6.2.1 Radiometric and polarimetric uncertainties

395 To examine the sensitivity of XCO_2 estimates to MAP radiometric and polarimetric uncertainties, we vary $\mathbf{S}_{y,MAP}$ in Equations (16) and (17) and perform the error analysis. As a starting point, we adopt a setup that is similar to SPEXone (Hasekamp et al., 2019). For this exercise, we assume 5 viewing angles at 0, ±40, ±60 degrees. The spectral range extends from 385 to 765 nm with a fixed radiance spectral resolution of 5 nm, and a DLP spectral resolution of 15 nm at 395 nm and 30nm at 765 nm. This spectral arrangement corresponds to 77 radiance and 19 DLP measurements. With 5 viewing angles, the total

400 number of measurements becomes 480. For each scenario, we compute $\langle \Delta XCO_2 \rangle$ that corresponds to each combination of 4 values of radiance uncertainties $\Delta I/I$ and 11 different values of DLP uncertainties ΔDLP. $\Delta I/I$ ranges from 1% to 4% and ΔDLP ranges from 0.001 to 0.05.
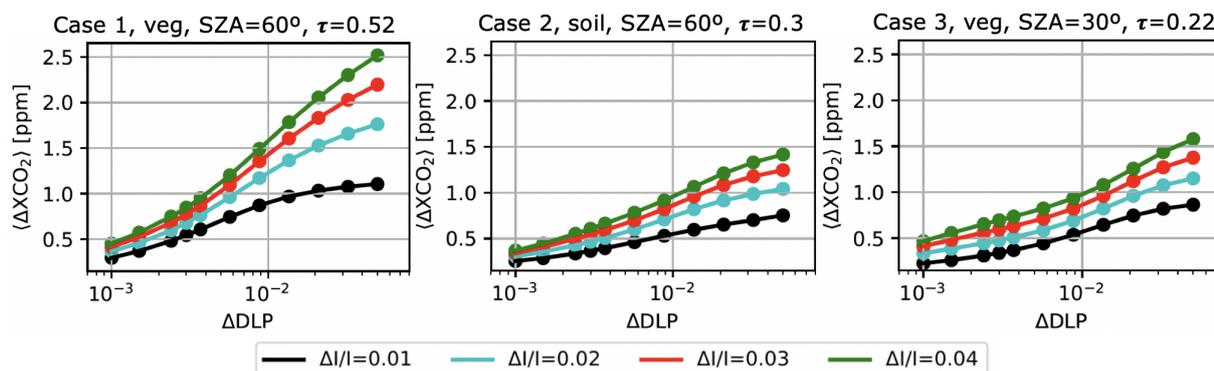
Figure 2. $\langle \Delta XCO_2 \rangle$ as a function of $\Delta I/I$ and ΔDLP, shown for scenarios where the errors are among the largest for each individual case 1,2, and 3. Here, τ indicates the sum of the fine- and the coarse-mode aerosol optical depth at 765 nm.

Figure 2 shows examples of $\langle \Delta XCO_2 \rangle$ for all combinations of $\Delta I/I$ and ΔDLP that we investigate. We present different sets of surface type, SZA, and τ that deliver among the largest $\langle \Delta XCO_2 \rangle$ in each aerosol case. The figure demonstrates that

405 XCO_2 uncertainties increase, as expected, with increasing DLP and radiance errors, and that holds true in all other scenarios as well. $\langle \Delta XCO_2 \rangle$ can be as high as ~ 2.4 ppm for the highest $\Delta I/I$ and ΔDLP considered here. It can be seen that the measurement errors that correspond to the allocated $\langle \Delta XCO_2 \rangle$ of 0.6 ppm are a combination of $\Delta I/I$ of about 2-3% and ΔDLP of around 0.003.

Figure 3 presents $\langle \Delta XCO_2 \rangle$ for all study scenarios when ΔDLP is fixed to 0.003, and compares the retrieval performance

410 between $\Delta I/I$ =2% and $\Delta I/I$ =3%. Generally speaking, the difference in $\langle \Delta XCO_2 \rangle$ for both $\Delta I/I$ values is relatively small. When radiance and DLP errors are not greater than 2% and 0.003, respectively, $\langle \Delta XCO_2 \rangle$ does not get higher than 0.6 ppm except for 3 scenarios; in most cases, $\langle \Delta XCO_2 \rangle$ is around or lower than 0.5 ppm. For $\Delta I/I$ of 3%, coupled with ΔDLP =0.003, $\langle \Delta XCO_2 \rangle$ increases beyond 0.6 ppm in a few scenarios by a relatively small margin. Among these scenarios, the highest
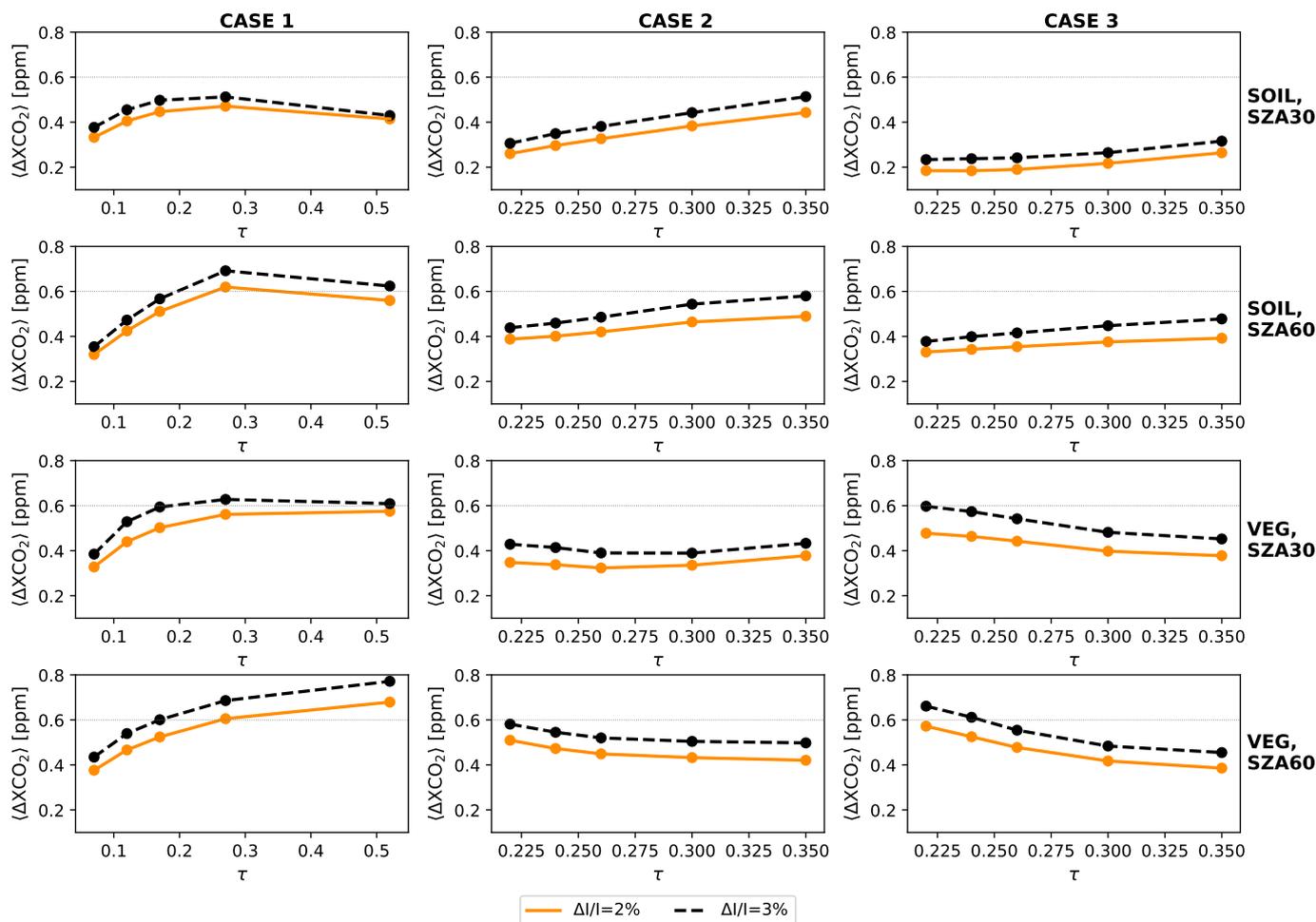
Figure 3. $\langle\Delta\mathrm{XCO_2}\rangle$ as a function of total aerosol optical depth at 765 nm for all 60 study scenarios. The two lines in each panel show $\langle\Delta\mathrm{XCO_2}\rangle$ for two different $\Delta I/I$ values, as computed for the MAP-mod concept with 5 viewing angles, where $\Delta\mathrm{DLP} = 0.003$ is assumed. The MAP-mod spectrum for each scenario extends from 385 to 765 nm.

$\langle\Delta\mathrm{XCO_2}\rangle$ is found for the case-1,vegetation,SZA$= 60°$,τ =0.52 scenario where it is just under 0.8 ppm; for the other scenarios, $\langle\Delta\mathrm{XCO_2}\rangle$ varies between 0.6-0.7 ppm. Given that the improvement in $\Delta I/I$ from 3% to 2% is a major technical challenge while the reduction in $\mathrm{XCO_2}$ uncertainty is only marginal, we adopt the more relaxed requirement here ($\Delta I/I$ =3% and $\Delta\mathrm{DLP}$ =0.003).

6.2.2 Number of viewing angles

If we change the number of viewing zenith angles (VZAs), we effectively add or remove measurements and this would certainly influence the aerosol and hence the $\mathrm{XCO_2}$ retrievals. A number of studies suggest that 5 viewing angles are sufficient for

aerosol retrieval (Hasekamp and Landgraf, 2007; Wu et al., 2015; Xu et al., 2017; Hasekamp et al., 2019). Here, we vary the number of viewing angles from 3 to 8, while keeping the spectral range and resolution the same as in section 6.2.1, resulting in 6 instrument setups to evaluate. For each scenario and each setup, $\mathbf{K_{MAP}}$ is computed. $\mathbf{S}_{y,MAP}$ is fixed, corresponding to $\Delta I/I$ =3% and ΔDLP =0.003. Table 5 lists the viewing angles and the corresponding number of measurements.

Table 5. List of the viewing angles in the evaluated MAP-mod setups

Number of VZAs	VZAs	Total number of measurements
3	0, ± 60	288
4	$\pm 19, \pm 57$	384
5	0, $\pm 40, \pm 60$	480
6	$\pm 12, \pm 36, \pm 60$	576
7	0, $\pm 20, \pm 40, \pm 60$	672
8	$\pm 8, \pm 25, \pm 42, \pm 60$	768

425   The resulting $\langle \Delta XCO_2 \rangle$ as a function of number of viewing angles is displayed in Figure 4. It shows that $\langle \Delta XCO_2 \rangle$ drops most sharply from 3 to 4 viewing angles in most cases. Cases 2 and 3 with SZA=60° show also a significant decline in $\langle \Delta XCO_2 \rangle$ from 4 to 5 viewing angles. Having more viewing angles beyond 5 lowers the aerosol-induced errors only marginally. For instance, having 8 viewing angles does not reduce $\langle \Delta XCO_2 \rangle$ to 0.6 ppm for the case-1,vegetation,SZA=60°,τ =0.52 scenario.

430   An odd number of viewing angles is preferred over an even number to allow for symmetry and to include a nadir view. Strictly speaking, a minimum of 7 viewing angles are required to have $\langle \Delta XCO_2 \rangle$ below 0.6 ppm for all study scenarios. However, 5 viewing angles deliver very similar $\langle \Delta XCO_2 \rangle$ and therefore meets our target aerosol-induced error for a vast majority of the study scenarios. Here we adopt 5 viewing angles as the required number of viewing angles.

6.2.3 Spectral range

435 Looking at heritage missions with different spectral coverage, we assess the effect of varying spectral range on the retrieved XCO_2 . Here we examine four options, i.e. (i) the same spectral range as in sections 6.2.1 and 6.2.2 ('default'), (ii) the default range including UV wavelengths down to 350nm ('with UV'), (iii) the default range without wavelengths shorter than 490 nm ('no UV'), (iv) the default range with 2 additional SWIR wavelengths 1640 and 2250 nm, at which both radiance and DLP measurements are taken ('with SWIR') . For each option, we assume 5 viewing angles at 0,$\pm$40,$\pm$60 degrees. For setups (i),
440   (ii), and (iii), the spectral resolutions for radiance and DLP are the same as those adopted in section 6.2.1, and the uncertainties are fixed to $\Delta I/I$ =3% and ΔDLP =0.003. Table 6 summarizes the four setups.

Figure 5 compares $\langle \Delta XCO_2 \rangle$ for the four spectral range options as a function of total aerosol optical depth. Compared to the default setup, it is apparent that adding more measurements in the UV leads to little gain in performance and that removing UV measurements altogether results in a considerably higher $\langle \Delta XCO_2 \rangle$. Without UV measurements, half of the scenarios
445   fail to meet the target 0.6 ppm; in some case-3,vegetation scenarios, $\langle \Delta XCO_2 \rangle$ even exceeds 1 ppm. The contribution of the
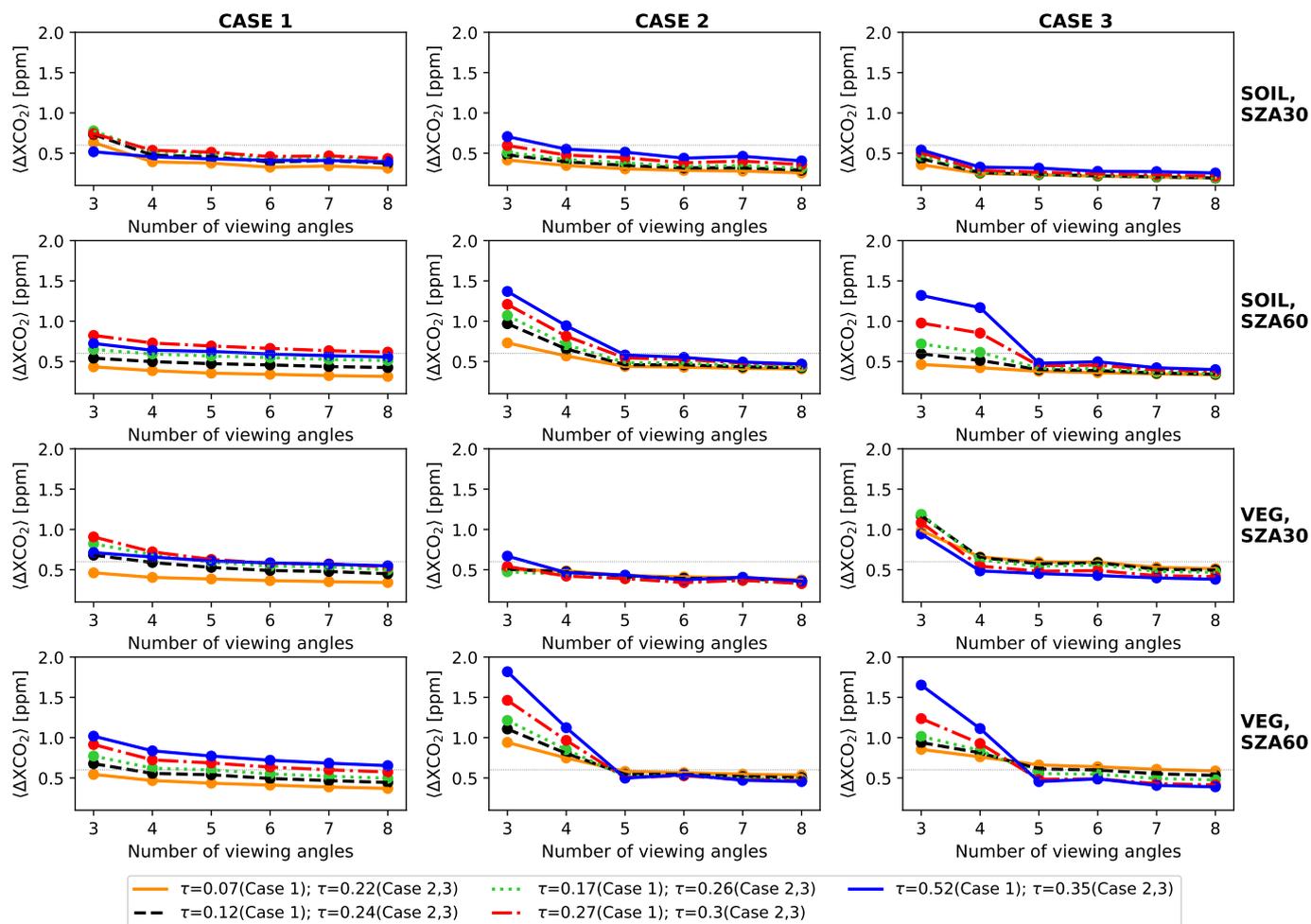
Figure 4. $\langle \Delta XCO_2 \rangle$ as a function of number of viewing angles for all 60 study scenarios. The 5 lines in each panel represent different values of total aerosol optical depth at 765 nm. $\langle \Delta XCO_2 \rangle$ is computed for the MAP-mod concept with $\Delta I/I$ =3% and ΔDLP =0.003. The MAP-mod spectrum for each scenario extends from 385 to 765 nm.

Table 6. List of the 4 options for the MAP-mod spectral range

Setup	Spectral range	Number of radiance measurements	Number of DLP measurements	Total number of measurements
default	385-765	77	19	480
with UV	350-765	84	22	530
no UV	490-765	56	12	340
with SWIR	385-2250	79	21	500
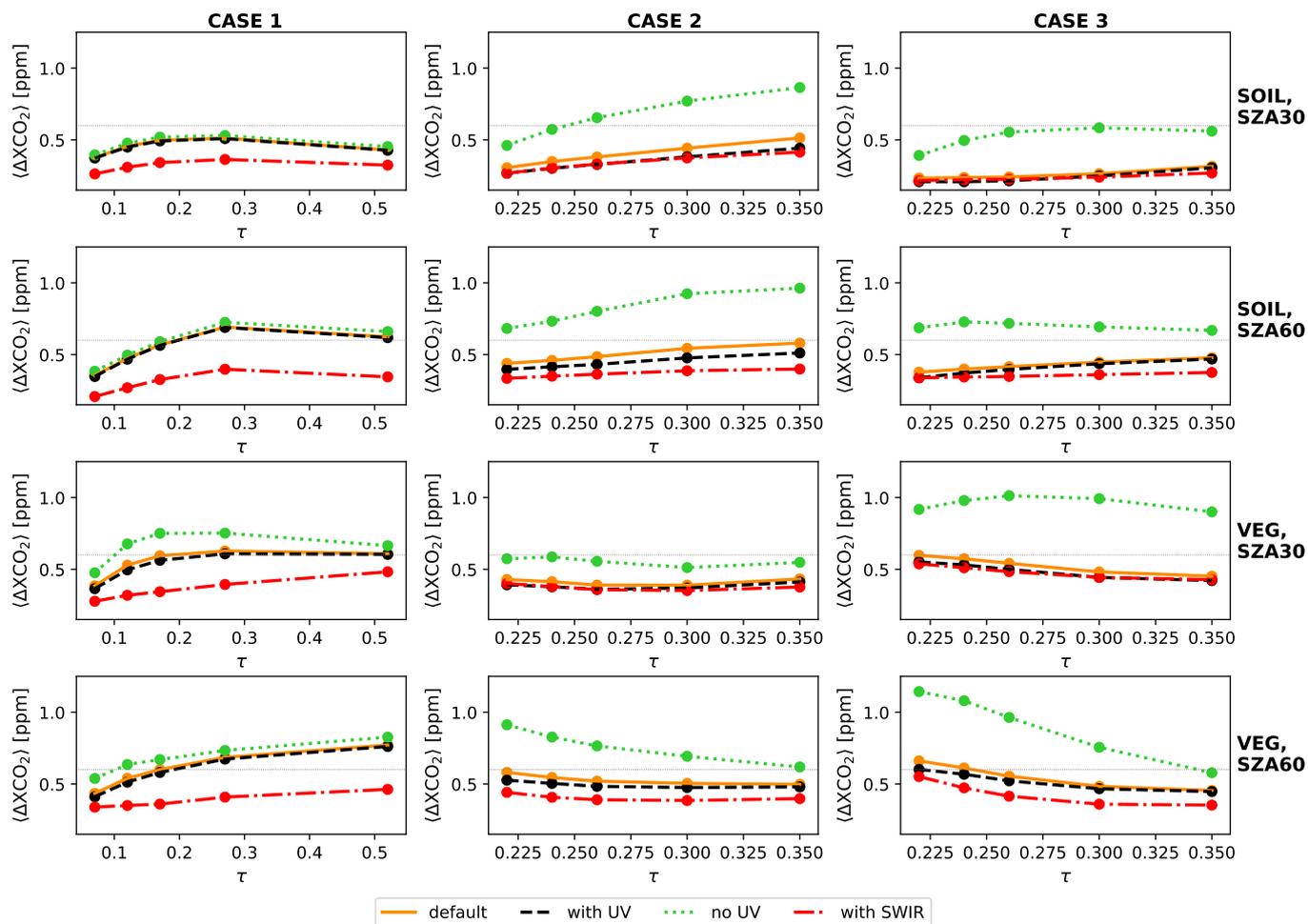
Figure 5. $\langle \Delta \mathrm{XCO_2} \rangle$ as a function of total aerosol optical depth at 765nm. The 4 lines in each panel represent 4 possible setups with different spectral range. $\langle \Delta \mathrm{XCO_2} \rangle$ is computed for the MAP-mod concept with 5 viewing angles, $\Delta I/I$ =3% and $\Delta \mathrm{DLP}$ =0.003.

two SWIR channels, as compared to the default spectral range, is most significant for case 1 scenarios in which a drop of $\langle \Delta \mathrm{XCO_2} \rangle$ up to ~ 0.3 ppm can be seen. For the other scenarios, the SWIR channels have only marginal effects. Given that for case 1 the default spectral range is already very close to the requirement, we conclude that the 'default' range (385-765 nm) is sufficient.

450   Following the assessment above, we adopt the default setup as the MAP-mod baseline setup. For clarity, we summarize this setup in Table 7.

Table 7. MAP-mod baseline setup

Features	Baseline setup
Number of VZAs	5
Viewing angles [degrees]	$0, \pm 40, \pm 60$
Spectral range	385-765 nm
Radiance spectral resolution	5 nm
DLP spectral resolution	15 at 395nm, 30 at 765nm
Number of radiance measurements	77
Number of DLP measurements	19
Total number of measurements	480
Radiance uncertainty	3%
DLP uncertainty	0.003

6.3 MAP-band instrument

For the MAP-band instrument, we consider 6 spectral bands from 410 to 865 nm, close to the 3MI VNIR polarized bands
(Fougnie et al., 2018), and we perform requirement analyses similar to those for MAP-mod. The study of Hasekamp and
455 Landgraf (2007) suggests that there is a strong overlap in angular and spectral information for aerosol retrieval, i.e. as long as
the total number of measurements is the same and there are at least 5 viewing angles, instruments with different number of
angles and wavelengths yield similar retrieval capability. This implies that the MAP band instrument with 40 viewing angles
can deliver a similar performance to MAP-mod, because the total number of measurements of the two concepts would then be
the same.

460 Figure 6 displays the performance of a MAP-band setup (40 viewing angles, 6 spectral bands, $\Delta I/I$ =3%, ΔDLP =0.003)
and the MAP-mod baseline setup. For most scenarios, $\langle \Delta \text{XCO}_2 \rangle$ delivered by both concepts are comparable, confirming what
is suggested in Hasekamp and Landgraf (2007). MAP-band fares somewhat poorly for scenarios with vegetation surface and
SZA=60°in cases 2 and 3. To maintain aerosol-induced errors at 0.6 ppm or lower for these scenarios, we find that the MAP-
band measurement uncertainties have to be unfeasibly low, i.e. $\Delta I/I$ must be 1% or less for a ΔDLP of 0.003, or alternatively,
465 ΔDLP must be less than 0.002 for a $\Delta I/I$ of 3%. The details of our proposed baseline setup for the MAP-band concept is
provided in Table 8.

7 XCO$_2$ retrieval using MAP and CO2M spectrometer measurements

The linear error analysis provides reliable XCO$_2$ error estimates assuming that the inversion problem has been succesfully
solved and the global minimum has been found. However, actual retrievals may have difficulties in achieving that and the
470 minimization procedure may get trapped in a local minimum. In this case, the real performance of the iterative retrievals would
be worse than that expected from the linear error analysis. For this reason, here we evaluate the retrieval capability of the
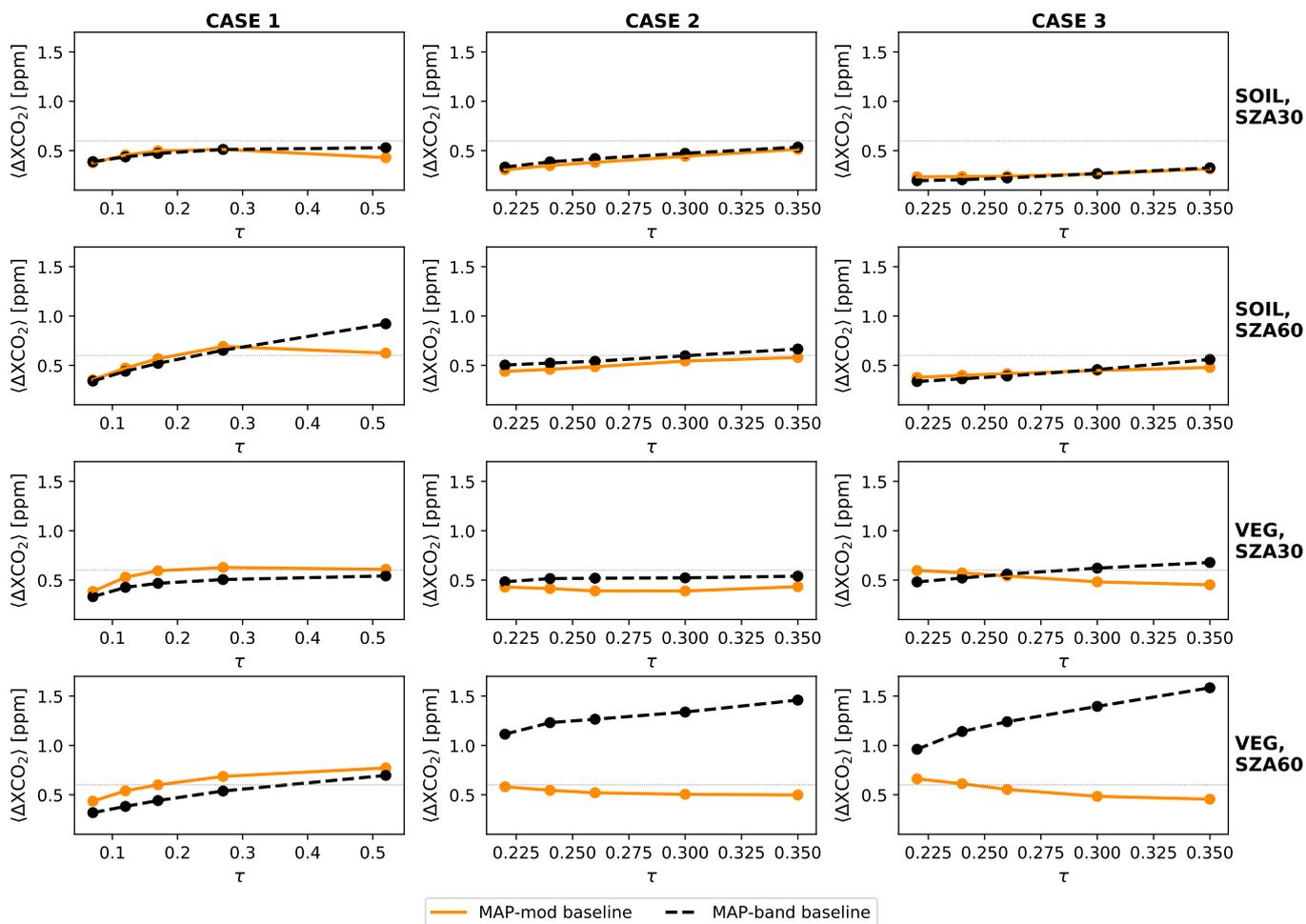
Figure 6. $\langle\Delta\mathrm{XCO_2}\rangle$ as a function of total aerosol optical depth at 765nm. The two lines in each panel represent the baseline setups of MAP-mod (orange, solid) and MAP-band (black, dashed).

combined spectrometer and MAP measurements using a full iterative approach (described in section 3.1) on a more diverse set of synthetic scenes. We adopt the baseline MAP-mod setup to simulate MAP observations and we consider the ensemble of 500 simulated scenes (as outlined in section 4) for this joint retrieval exercise.

475   We apply the same χ^2 filtering as in section 5 to the joint retrieval results. Out of the 500 scenes, 349 (70%) with $\chi^2 \leq 1.5$ are left and their $\Delta\mathrm{XCO_2}$ are evaluated. Higher convergence rates can potentially be achieved with further refinements of the iterative scheme and a better approach to select the first guess state vector. As in section 5, $\Delta\mathrm{XCO_2}$ is the difference between the retrieved and the true $\mathrm{XCO_2}$. Since random instrument errors are added to the simulated spectra, $\Delta\mathrm{XCO_2}$ here is a combination of aerosol-induced errors (which include MAP instrument noise) and spectrometer-noise-induced errors.

Table 8. MAP-band baseline setup

Features	Baseline setup
Number of VZAs	40
Viewing angles [degrees]	$\pm2, \pm5, \pm8, \pm11, ..., \pm54, \pm57, \pm60$
Wavelengths [nm]†	410, 440, 490, 550, 669.9, 863.4
Number of radiance measurements	240
Number of DLP measurements	240
Total number of measurements	480
Radiance uncertainty	3%
DLP uncertainty	0.003

† In the official baseline setup for the MAP-band instrument, the list of spectral
bands includes 753 nm. The channel is added for calibration purposes, owing
to its overlap with the NIR band of the CO2M spectrometer. Only radiance
measurements are taken in this channel, therefore we do not consider it in our
analysis.

Figure 7 plots ΔXCO_2 for the 349 converged retrievals as a function of the true values of aerosol optical depth and height, SZA, and albedo. The range of ΔXCO_2 values along the y-axis is kept the same as in Figure 1 for easy comparison. A few things that stand out from comparing the two figures are the substantial reduction in ΔXCO_2 scatter and the absence of strong XCO_2 bias in the joint retrieval results. Excluding a few obvious outliers, the general trends are as follows. As the aerosol optical depth gets higher, the scatter of ΔXCO_2 increases only mildly with no signs of significant overestimation or underestimation of the retrieved XCO_2 . With respect to the aerosol altitude, ΔXCO_2 scatter is practically unchanged with almost no bias visible at any height. As for the SZA, a slightly larger scatter of ΔXCO_2 is observed starting SZA$\sim 60°$with no particular collective offset across the whole range of SZA. For the albedo, the scatter of ΔXCO_2 is maintained over the range considered here.

As done for the spectrometer-only retrieval results, we again choose to adopt the median and P_{SD} as a measure of the retrieval bias and the spread of ΔXCO_2 distribution. From the 349 converged retrievals, the bias is -0.004 ppm and the spread is 0.54 ppm. The latter is consistent with what we expect from the linear error analysis for the MAP-mod baseline setup (see e.g. Figure 6). More importantly, 0.54 ppm lies well within the CO2M total error budget (0.86 ppm) and therefore compliant with the mission requirements.

Compared to the statistics of the spectrometer-only retrievals, the joint retrieval results obviously represent a major improvement in the accuracy and precision of the retrieved XCO_2 . The retrieval bias is reduced by more than two orders of magnitude and the scatter is lowered by almost a factor of 4. The smaller bias and scatter imply that a higher number of observed scenes can be processed into reliable estimates of XCO_2 . Moreover, the absence of ΔXCO_2 correlations with aerosol optical depth, aerosol height, and SZA means there is a minimal risk of regional biases in the L2-products, driven by variations
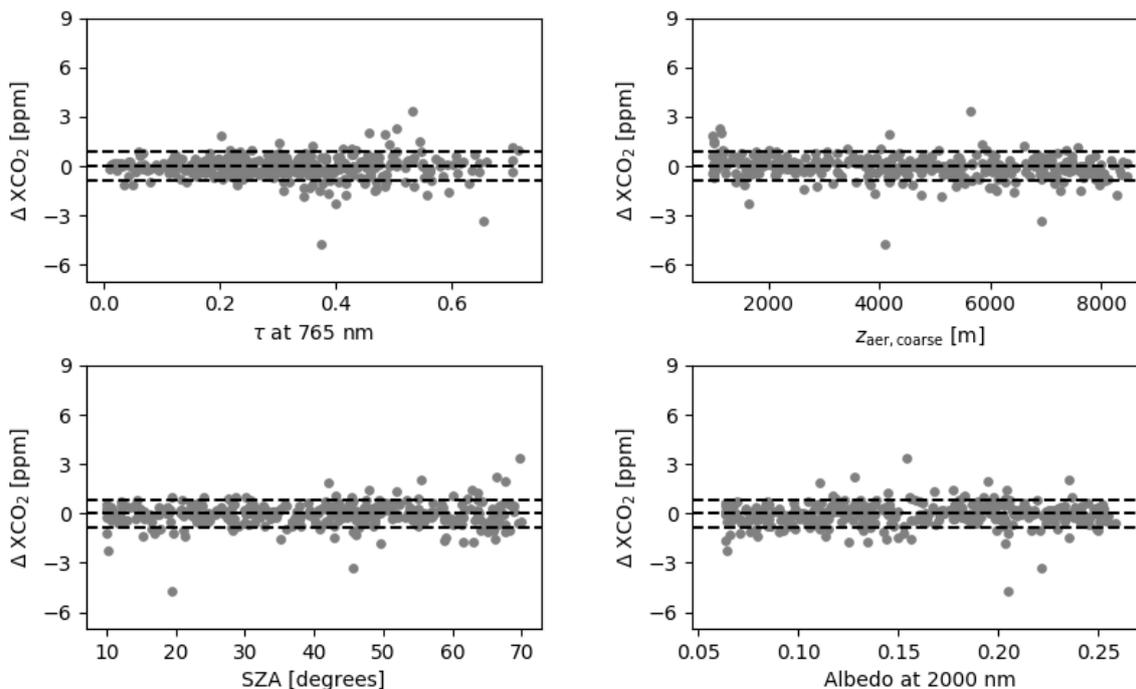
Figure 7. Residual XCO_2 from the converged retrievals using spectrometer and MAP measurements, shown as a function of total aerosol optical depth τ , coarse-mode aerosol height, SZA, and albedo. The input spectra are generated according to the ensemble of synthetic scenes (Section 4). The three dashed horizontal lines indicate ΔXCO_2 at -0.86, 0, and 0.86 ppm.

in aerosol properties and SZA. Altogether, such improvements will lead to a higher data yield, better global coverage and a
500 more comprehensive determination of CO_2 sinks and sources.

Deployment of a MAP instrument would additionally offer a better insight into the surface reflection properties, which are important factors in simulating the radiation at the top of atmosphere, especially for retrievals over land. In section 5, the simulated spectrometer spectra and the eventual retrieval are based on a Lambertian description of the surface. In reality, the Lambertian assumption does not hold and this would likely lower the XCO_2 accuracy of the spectrometer-only retrievals even
505 further, particularly for cases with larger aerosol optical depth because of multiple light scattering between the surface and aerosol particles.

8 Summary

In the context of ESA's CO2M mission, we investigated the need for an aerosol-dedicated instrument (multi-angle polarimeter or MAP) in support of the CO2M spectrometer to achieve the required XCO_2 accuracy and precision. We estimated aerosol-
510 induced XCO_2 errors from two XCO_2 retrieval approaches on an ensemble of 500 synthetic scenes over land. The first approach represents a customary way to account for aerosol effects on the retrieved XCO_2 using only measurements of a 3-

band spectrometer. The second strategy incorporates MAP and spectrometer measurements in a synergistic way to retrieve XCO_2 (joint retrieval).

In the ensemble of synthetic scenes, aerosol size distribution is described by a bimodal lognormal function, where each mode
515 follows a Gaussian height distribution. The trace gas total column, aerosol and surface properties, and the solar zenith angle are randomly varied within certain limits to generate 500 atmospheric and geophysical scenes.

For the standard retrieval exercise using only spectrometer data, we employed the RemoTeC algorithm that has been widely used for greenhouse gas retrievals from space. In RemoTeC, a simple aerosol model is used, i.e. aerosol size distribution is retrieved following a monomodal power-law parametrization. Out of 500 retrievals, 69% meet our χ^2 convergence criterion.
520 The median value of the residual XCO_2 (ΔXCO_2) from the converged retrievals is 1.12 ppm and the spread is 2.07 ppm. Given that the total XCO_2 error budget of the CO2M mission is 0.86 ppm (the quadratic sum of the required XCO_2 accuracy of 0.5 ppm and the required XCO_2 precision of 0.7 ppm), the results show that the standard retrieval approach is greatly inadequate and does not comply with the mission requirements. Furthermore, the retrieval performance is markedly degraded at high aerosol optical depth, high aerosol altitude and low SZA. This may lead to biases in determining CO_2 emissions from
525 polluted areas where CO_2 and aerosols are co-emitted.

Prior to performing the joint retrieval, we conducted a requirement analysis to construct a baseline setup for each of the two alternative MAP concepts being considered for the CO2M mission, i.e. MAP-mod and MAP-band. The MAP-mod concept is based on a spectral modulation technique where polarization information is encoded in the modulation pattern of the radiance spectrum, while the MAP-band instrument acquires radiance and polarization measurements at specific discrete spectral bands.
530 The MAP-mod instrument inherits from SPEXone and the MAP-band wavelength channels inherit from 3MI polarized VNIR bands. The optimal baseline setups for the MAP-mod and for the MAP-band instrument designs are found through a linear error analysis that is formulated to mimic a joint retrieval. In particular, we investigated three aspects of a MAP instruments, i.e. the measurement uncertainties, number of viewing angles, and wavelength range. For the MAP-mod concept, the baseline setup includes 5 viewing angles ($\pm60°,\pm40°,0°$), 77 radiance measurements (with $\Delta I/I$ =3%) and 19 DLP measurements
535 (with ΔDLP =0.003) ranging from 385 nm to 765 nm. The baseline setup for the MAP-band concept requires 40 viewing angles (from -60°to 60°), 6 spectral bands between 410 and 865 nm at which both radiances and DLP are measured, with the same radiometric and polarimetric uncertainty requirements as for the MAP-mod baseline. The baseline setups of MAP-mod and MAP-band have generally similar performance.

To implement the joint retrieval, we further developed an existing aerosol retrieval algorithm to include features related to the
540 spectrometer measurements and to the derivation of trace gas total columns. Using this retrieval tool, 70% of the 500 retrievals reach convergence according to our χ^2 criterion. Of the converged ones, the median ΔXCO_2 is found at -0.004 ppm, and the spread stands at 0.54 ppm, which is consistent with what is expected from the linear error analysis for the MAP-mod baseline setup. More importantly, 0.54 ppm fits well within the CO2M XCO_2 error budget of 0.86 ppm and therefore is compliant with the CO2M requirements. There is not any appreciable correlation in our test ensemble between ΔXCO_2 with the aerosol
545 optical depth, aerosol height, solar zenith angle, or albedo.

The results of the joint retrieval represent a significant improvement in the retrieved XCO_2 accuracy with respect to the standard retrieval approach using a 3-band spectrometer only. The bias and the scatter of ΔXCO_2 are much smaller in the joint retrieval, which would ultimately translate to better estimates of CO_2 sinks and sources. Figure 8 concisely sums up the main results of this study. It shows to a large extent the benefit of having MAP observations to support XCO_2 retrieval. It shows that

550   MAP observations are indispensable in minimizing aerosol-induced XCO_2 errors and in achieving the XCO_2 precision and accuracy required by the CO2M mission.
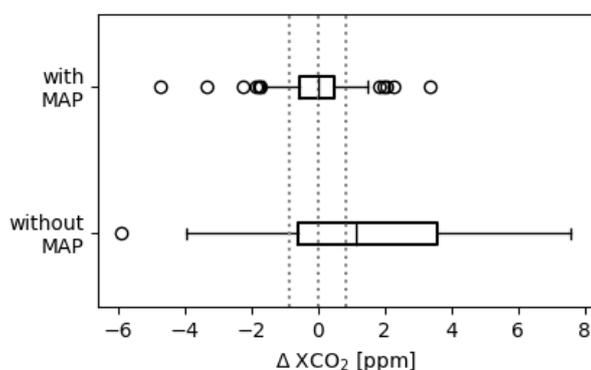
Figure 8. Boxplot of ΔXCO_2 from retrievals of the synthetic scenes using 3-band spectrometer measurements only ('without MAP') versus those from retrievals using the combined MAP and spectrometer data ('with MAP'). The rectangles are outlined by the 15.9th and the 84.1th percentiles (P(15.9) and P(84.1)) with the 50th percentile (median) indicated by a vertical line inside the rectangles. The length of the whiskers are set to the difference between P(84.1) and P(15.9). The circles indicate retrievals with ΔXCO_2 beyond the extent of the whiskers. The three dotted vertical lines mark -0.86, 0, and 0.86 ppm.

Appendix A: Lognormal distribution

The lognormal distribution is used in this paper to describe the size distribution $n(r)$ of each aerosol mode. It reads as follows:

$$n(r) = \frac{1}{r \ln s_g \sqrt{2\pi}} \exp\left[-\frac{(\ln r - \ln r_m)^2}{2(\ln s_g)^2}\right], \tag{A1}$$

with r, r_m and s_g being radius, median radius and the geometric standard deviation. Here, we use effective radius r_{eff} and effective variance v_{eff} in place of r_m and s_g, where

$$v_{\text{eff}} = \exp((\ln s_g)^2) - 1, \tag{A2}$$

$$r_{\text{eff}} = r_m(1 + v_{\text{eff}})^{2.5}. \tag{A3}$$

References

Aben, I., Hasekamp, O., and Hartmann, W.: Uncertainties in the space-based measurements of CO_2 columns due to scattering in the Earth's atmosphere, J. Quant. Spectrosc. Radiat. Transfer, 104, 450–459, https://doi.org/10.1016/j.jqsrt.2006.09.013, 2007.

Basilio, R. R., Bennett, M. W., Eldering, A., Lawson, P. R., and Rosenberg, R. A.: Orbiting Carbon Observatory-3 (OCO-3), remote sensing from the International Space Station (ISS), in: Sensors, Systems, and Next-Generation Satellites XXIII, edited by Neeck, S. P., Martimort, P., and Kimura, T., vol. 11151, pp. 42 – 55, International Society for Optics and Photonics, SPIE, https://doi.org/10.1117/12.2534996, https://doi.org/10.1117/12.2534996, 2019.

Bucholtz, A.: Rayleigh-Scattering calculations for the terrestrial atmosphere, Appl. Opt., 35, 2765–2773, 1995.

Butz, A., Hasekamp, O. P., Frankenberg, C., and Aben, I.: Retrievals of atmospheric CO_2 from simulated space-borne measurements of backscattered near-infrared sunlight: accounting for aerosol effects, Appl. Opt., 48, 3322, https://doi.org/10.1364/AO.48.003322, 2009.

Butz, A., Hasekamp, O. P., Frankenberg, C., Vidot, J., and Aben, I.: CH_4 retrievals from space-based solar backscatter measurements: Performance evaluation against simulated aerosol and cirrus loaded scenes, J. Geophys. Res., 115, D24 302, https://doi.org/10.1029/2010JD014514, 2010.

Butz, A., Guerlet, S., Hasekamp, O., Schepers, D., Galli, A., Aben, I., Frankenberg, C., Hartmann, J. M., Tran, H., Kuze, A., Keppel-Aleks, G., Toon, G., Wunch, D., Wennberg, P., Deutscher, N., Griffith, D., Macatangay, R., Messerschmidt, J., Notholt, J., and Warneke, T.: Toward accurate CO_2 and CH_4 observations from GOSAT, Geophys. Res. Lett., 38, doi:10.1029/2011GL047 888, 2011.

Butz, A., Galli, A., Hasekamp, O., Landgraf, J., Tol, P., and I., A.: TROPOMI aboard Sentinel-5 Precursor: Prospective performance of CH4 retrievals for aerosol and cirrus loaded atmospheres, Remote Sens. Envirom., 120, 267, 2012.

Ciais, P., Dolman, A. J., Bombelli, A., Duren, R., Peregon, A., Rayner, P. J., Miller, C., Gobron, N., Kinderman, G., Marland, G., Gruber, N., Chevallier, F., Andres, R. J., Balsamo, G., Bopp, L., Bréon, F. M., Broquet, G., Dargaville, R., Battin, T. J., Borges, A., Bovensmann, H., Buchwitz, M., Butler, J., Canadell, J. G., Cook, R. B., DeFries, R., Engelen, R., Gurney, K. R., Heinze, C., Heimann, M., Held, A., Henry, M., Law, B., Luyssaert, S., Miller, J., Moriyama, T., Moulin, C., Myneni, R. B., Nussli, C., Obersteiner, M., Ojima, D., Pan, Y., Paris, J. D., Piao, S. L., Poulter, B., Plummer, S., Quegan, S., Raymond, P., Reichstein, M., Rivier, L., Sabine, C., Schimel, D., Tarasova, O., Valentini, R., Wang, R., van der Werf, G., Wickland, D., Williams, M., and Zehner, C.: Current systematic carbon-cycle observations and the need for implementing a policy-relevant carbon observing system, Biogeosciences, 11, 3547–3602, https://doi.org/10.5194/bg-11-3547-2014, 2014.

Ciais, P., Crisp, D., van der Gon, H. D., Engelen, R., Janssens-Maenhout, G., Heimann, M., Rayner, P., and Scholze, M.: Towards a European operational observing system to monitor fossil CO_2 emissions, Final Report from the expert group, European Comission, 2015.

Crisp, D., Meijer, Y., Munro, R., Bowman, K., Chatterjee, A., Baker, D., Chevallier, F., Nassar, R., Palmer, P., Agusti-Panareda, A., Al-Saadi, J., Ariel, Y., Basu, S., Bergamaschi, P., Boesch, H., Bousquet, P., Bovensmann, H., Bréon, F.-M., Brunner, D., Buchwitz, M., Buisson, F., Burrows, J., Butz, A., Ciais, P., Clerbaux, C., Counet, P., Crevoisier, C., Crowell, S., DeCola, P., Deniel, C., Dowell, M., Eckman, R., Edwards, D., Ehret, G., Eldering, A., Engelen, R., Fisher, B., Germain, S., Hakkarainen, J., Hilsenrath, E., Holmlund, K., Houweling, S., Hu, H., Jacob, D., Janssens-Maenhout, G., Jones, D., Jouglet, D., Kataoka, F., Kiel, M., Kulawik, S., Kuze, A., Lachance, R., Lang, R., Landgraf, J., Liu, J., Liu, Y., Maksyutov, S., Matsunaga, T., McKeever, J., Moore, B., Nakajima, M., Natraj, V., Nelson, R., Niwa, Y., Oda, T., O'Dell, C., Ott, L., Patra, P., Pawson, S., Payne, V., Pinty, B., Polavarapu, S., Retscher, C., Rosenberg, R., Schuh, A., Schwandner, F., Shiomi, K., Su, W., Tamminen, J., Taylor, T., Veefkind, P., Veihelmann, B., Wofsy, S., Worden, J., Wunch, D., Yang, D., Zhang, P.,

and Zehner, C.: A Constellation Architecture for Monitoring CArbon Dioxide and Methane from Space, Report, Committee on Earth Observation Satellites, 2018.

Deschamps, P. Y., Breon, F. M., Leroy, M., Podaire, A., Bricaud, A., Buriez, J. C., and Seze, G.: The POLDER mission: instrument characteristics and scientific objectives, IEEE Transactions on Geoscience and Remote Sensing, 32, 598–615, https://doi.org/10.1109/36.297978, 1994.

Diner, D. J., Boland, S. W., Brauer, M., Bruegge, C., Burke, K. A., Chipman, R., Di Girolamo, L., Garay, M. J., Hasheminassab, S., Hyer, E., Jerrett, M., Jovanovic, V., Kalashnikova, O. V., Liu, Y., Lyapustin, A. I., Martin, R. V., Nastan, A., Ostro, B. D., Ritz, B., Schwartz, J., Wang, J., and Xu, F.: Advances in multiangle satellite remote sensing of speciated airborne particulate matter and association with adverse health effects: from MISR to MAIA, Journal of Applied Remote Sensing, 12, 042603, https://doi.org/10.1117/1.JRS.12.042603, 2018.

Dubovik, O., Sinyuk, A., Lapyonok, T., Holben, B. N., Mishchenko, M., Yang, P., Eck, T. F., Volten, H., MuñOz, O., Veihelmann, B., van der Zande, W. J., Leon, J.-F., Sorokin, M., and Slutsker, I.: Application of spheroid models to account for aerosol particle nonsphericity in remote sensing of desert dust, J. Geophys. Res., 111, D11 208, https://doi.org/10.1029/2005JD006619, 2006.

Dubovik, O., Li, Z., Mishchenko, M. I., Tanré, D., Karol, Y., Bojkov, B., Cairns, B., Diner, D. J., Espinosa, W. R., Goloub, P., Gu, X., Hasekamp, O., Hong, J., Hou, W., Knobelspiesse, K. D., Landgraf, J., Li, L., Litvinov, P., Liu, Y., Lopatin, A., Marbach, T., Maring, H., Martins, V., Meijer, Y., Milinevsky, G., Mukai, S., Parol, F., Qiao, Y., Remer, L., Rietjens, J., Sano, I., Stammes, P., Stamnes, S., Sun, X., Tabary, P., Travis, L. D., Waquet, F., Xu, F., Yan, C., and Yin, D.: Polarimetric remote sensing of atmospheric aerosols: Instruments, methodologies, results, and perspectives, J. Quant. Spectrosc. Radiat. Transfer, 224, 474–511, https://doi.org/10.1016/j.jqsrt.2018.11.024, 2019.

Fougnie, B., Marbach, T., Lacan, A., Lang, R., Schlüssel, P., Poli, G., Munro, R., and Couto, A. B.: The multi-viewing multi-channel multi-polarisation imager - Overview of the 3MI polarimetric mission for aerosol and cloud characterization, jqsrt, 219, 23–32, https://doi.org/10.1016/j.jqsrt.2018.07.008, 2018.

Fu, G. and Hasekamp, O.: Retrieval of aerosol microphysical and optical properties over land using a multimode approach, Atmospheric Measurement Techniques, 11, 6627–6650, https://doi.org/10.5194/amt-11-6627-2018, 2018.

Fu, G., Hasekamp, O., Rietjens, J., Smit, M., Di Noia, A., Cairns, B., Wasilewski, A., Diner, D., Seidel, F., Xu, F., Knobelspiesse, K., Gao, M., da Silva, A., Burton, S., Hostetler, C., Hair, J., and Ferrare, R.: Aerosol retrievals from different polarimeters during the ACEPOL campaign using a common retrieval algorithm, Atmospheric Measurement Techniques, 13, 553–573, https://doi.org/10.5194/amt-13-553-2020, 2020.

Guerlet, S., Butz, A., Schepers, D., Basu, S., Hasekamp, O. P., Kuze, A., Yokota, T., Blavier, J.-F., Deutscher, N. M., Griffith, D. W. T., Hase, F., Kyro, E., Morino, I., Sherlock, V., Sussmann, R., Galli, A., and Aben, I.: Impact of aerosol and thin cirrus on retrieving and validating XCO_2 from GOSAT shortwave infrared measurements, J. Geophys. Res., 118, 4887–4905, https://doi.org/10.1002/jgrd.50332, 2013.

Hasekamp, O. and Landgraf, J.: A linearized vector radiative transfer model for atmospheric trace gas retrieval, J. Quant. Spectrosc. Radiat. Transfer, 75, 2002.

Hasekamp, O. P. and Butz, A.: Efficient calculation of intensity and polarization spectra in vertically inhomogeneous scattering and absorbing atmospheres, J. Geophys. Res., 113, D20 309, https://doi.org/10.1029/2008JD010379, 2008.

Hasekamp, O. P. and Landgraf, J.: Linearization of vector radiative transfer with respect to aerosol properties and its use in satellite remote sensing, J. Geophys. Res., 110, D04 203, https://doi.org/10.1029/2004JD005260, 2005.

Hasekamp, O. P. and Landgraf, J.: Retrieval of aerosol properties over land surfaces: capabilities of multiple-viewing-angle intensity and polarization measurements, Applied Optics, 46, 3332–3344, https://doi.org/10.1364/AO.46.003332, 2007.

Hasekamp, O. P., Litvinov, P., and Butz, A.: Aerosol properties over the ocean from PARASOL multiangle photopolarimetric measurements, Journal of Geophysical Research (Atmospheres), 116, D14204, https://doi.org/10.1029/2010JD015469, 2011.

Hasekamp, O. P., Fu, G., Rusli, S. P., Wu, L., Di Noia, A., Brugh, J. a. d., Landgraf, J., Martijn Smit, J., Rietjens, J., and van Amerongen, A.: Aerosol measurements by SPEXone on the NASA PACE mission: expected retrieval capabilities, jqsrt, 227, 170–184, https://doi.org/10.1016/j.jqsrt.2019.02.006, 2019.

Houweling, A., Hartmann, W., Aben, I., Schrijver H., Skidmore, J., Roelofs, G.-J., and F.-M., B.: Evidence of systematic errors in SCIAMACHY-observed CO2 due to aerosols, Atmos. Meas. Tech., 5, 2005.

Hu, H., Hasekamp, O., Butz, A., Galli, A., Landgraf, J., Aan de Brugh, J., Borsdorff, T., Scheepmaker, R., and Aben, I.: The operational methane retrieval algorithm for TROPOMI, Atmospheric Measurement Techniques, 9, 5423–5440, https://doi.org/10.5194/amt-9-5423-2016, 2016.

Jung, Y., Kim, J., Kim, W., Boesch, H., Lee, H., Cho, C., and Goo, T.-Y.: Impact of Aerosol Property on the Accuracy of a CO2 Retrieval Algorithm from Satellite Remote Sensing, Remote Sensing, 8, 322, https://doi.org/10.3390/rs8040322, 2016.

Kuang, Z., Margolis, J., Toon, G., Crisp, D., and Yung, Y.: Spaceborne measurements of atmospheric CO_2 by high-resolution NIR spectrometry of reflected sunlight: An introductory study, Geophys. Res. Lett., 29, 1716, https://doi.org/10.1029/2001GL014298, 2002.

Kuhlmann, G., Broquet, G., Marshall, J., Clément, V., Löscher, A., Meijer, Y., and Brunner, D.: Detectability of CO_2 emission plumes of cities and power plants with the Copernicus Anthropogenic CO_2 Monitoring (CO2M) mission, Atmospheric Measurement Techniques Discussions, 2019, 1–35, https://doi.org/10.5194/amt-2019-180, https://www.atmos-meas-tech-discuss.net/amt-2019-180/, 2019.

Landgraf, J., Hasekamp, O., Box, M., and Trautmann, T.: A Linearized Radiative Transfer Model Using the Analytical Perturbation Approach, J. Geophys. Res., 106, 27 291–27 305, 2001.

Litvinov, P., Hasekamp, O., and Cairns, B.: Models for surface reflection of radiance and polarized radiance: Comparison with airborne multiangle photopolarimetric measurements and implications for modeling top-of-atmosphere measurements, Remote Sensing of Environment, 115, 781–792, https://doi.org/10.1016/j.rse.2010.11.005, 2011.

Maignan, F., Bréon, F.-M., Fédèle, E., and Bouvier, M.: Polarized reflectances of natural surfaces: Spaceborne measurements and analytical modeling, Remote Sensing of Environment, 113, 2642–2650, https://doi.org/10.1016/j.rse.2009.07.022, 2009.

Martins, J. V., Fernandez-Borda, R., McBride, B., Remer, L., and Barbosa, H. M. J.: The Harp hyperangular imaging polarimeter and the need for small satellite payloads with high science payoff for earth science remote sensing, IEEE International Geoscience and Remote Sensing Symposium, pp. 6304–6307, 2018.

Meijer, Y., Boesch, H., Bombelli, A., Brunner, D., Buchwitz, M., Ciais, P., Crips, D., Engenlen, R., Holmlund, K., Houweling, S., Janssens-Maenhout, G., Marshall, J., Nakajima, M., Pinty, B., Scholze, M., Bezy, J. L., Drinkwater, M. R., Fehr, T., Fernandez, V., Loescher, A., Nett, H., Sierk, B., Dubovik, O., Landgraf, J., Lang, R., Lindqvist, H., Tamminen, J., and Veefkind, P.: Copernicus CO_2 Monitoring Mission Requirements Document, Earth and Mission Science Division, European Space Agency, 2019.

Mishchenko, M. I., Geogdzhayev, I. V., Cairns, B., Rossow, W. B., and Lacis, A. A.: Aerosol retrievals over the ocean by use of channels 1 and 2 AVHRR data: sensitivity analysis and preliminary results, Applied Optics, 38, 7325–7341, https://doi.org/10.1364/AO.38.007325, 1999.

Morino, I., Uchino, O., Inoue, M., Yoshida, Y., Yokota, T., Wennberg, P. O., Toon, G. C., Wunch, D., Roehl, C. M., Notholt, J., Warneke, T., Messerschmidt, J., Griffith, D. W. T., Deutscher, N. M., Sherlock, V., Connor, B., Robinson, J., Sussmann, R., and Rettinger, M.: Preliminary validation of column-averaged volume mixing ratios of carbon dioxide and methane retrieved from GOSAT short-wavelength infrared spectra, Atmospheric Measurement Techniques, 4, 1061–1076, https://doi.org/10.5194/amt-4-1061-2011, 2011.

Nelson, R. R. and O'Dell, C. W.: The impact of improved aerosol priors on near-infrared measurements of carbon dioxide, Atmospheric Measurement Techniques, 12, 1495–1512, https://doi.org/10.5194/amt-12-1495-2019, 2019.

Oshchepkov, S., Bril, A., and Yokota, T.: PPDF-based method to account for atmospheric light scattering in observations of carbon dioxide from space, J. Geophys. Res., 113, D23 210, https://doi.org/10.1029/2008JD010061, 2008.

Phillips, P.: A technique for the numerical solution of certain integral equations of the first kind, J. Ass. Comput. Mat., 9, 84–97, 1962.

Pinty, B., Janssens-Maenhout, G., Dowell, M., Zunker, H., Brunhes, T., Ciais, P., Dee, D., van der Gon, H. D., Dolman, H., Drinkwater, M., Engelen, R., Heimann, M., Holmlund, K., Husband, R., Kentarchos, A., Meijer, Y., Palmer, P., and Scholze, M.: An Operational Anthropogenic CO_2 Emissions Monitoring & Verification Support capacity - Baseline Requirements, Model Components and Functional Architecture, European Commission Joint Research Centre, https://doi.org/10.2760/39384, 2017.

Reuter, M., Buchwitz, M., Schneising, O., Noël, S., Bovensmann, H., and Burrows, J.: A Fast Atmospheric Trace Gas Retrieval for Hyperspectral Instruments Approximating Multiple Scattering—Part 2: Application to XCO2 Retrievals from OCO-2, Remote Sensing, 9, 1102, https://doi.org/10.3390/rs9111102, 2017.

Rietjens, J. H. H., Smit, M., van Harten, G., Di Noia, A., Hasekamp, O. P., de Boer, J., Volten, H., Snik, F., and Keller, C. U.: Accurate spectrally modulating polarimeters for atmospheric aerosol characterization, vol. 9613 of *Society of Photo-Optical Instrumentation Engineers (SPIE) Conference Series*, p. 96130S, https://doi.org/10.1117/12.2188024, 2015.

Rodgers, C.: Inverse Methods for Atmospheres: Theory and Practice, vol. 2, World Scientific, 2000.

Rothman, L., Gordon, I., Barbe, A., and et al.: The HITRAN 2008 molecular spectroscopic database, J. Quant. Spectrosc. Radiat. Transfer, 110, 533–572, 2009.

Scheepmaker, R. A., Frankenberg, C., Galli, A., Butz, A., Schrijver, H., Deutscher, N. M., Wunch, D., Warneke, T., Fally, S., and Aben, I.: Improved water vapour spectroscopy in the 4174–4300 cm^{-1} region and its impact on SCIAMACHY HDO/H_2O measurements, Atmos. Meas. Tech., 6, 879–894, https://doi.org/10.5194/amt-6-879-2013, http://www.atmos-meas-tech.net/6/879/2013/, 2013.

Snik, F., Karalidi, T., and Keller, C. U.: Spectral modulation for full linear polarimetry, aopt, 48, 1337–1346, https://doi.org/10.1364/AO.48.001337, 2009.

Tanré, D., Bréon, F. M., Deuzé, J. L., Dubovik, O., Ducos, F., François, P., Goloub, P., Herman, M., Lifermann, A., and Waquet, F.: Remote sensing of aerosols by using polarized, directional and spectral measurements within the A-Train: the PARASOL mission, Atmospheric Measurement Techniques, 4, 1383–1395, https://doi.org/10.5194/amt-4-1383-2011, 2011.

Tikhonov, A.: On the solution of incorrectly stated problems and a method of regularization, Dokl. Acad. Nauk SSSR, 151, 501–504, 1963.

Tran, H., Boulet, C., and Hartmann, J.-M.: Line mixing and collision-induced absorption by oxygen in the A band: Laboratory measurements, model, and tools for atmospheric spectra computations, J. Geophys. Res., 111, D15210, https://doi.org/10.1029/2005JD006869, 2006.

Wanner, W., Li, X., and Strahler, A. H.: On the derivation of kernels for kernel-driven models of bidirectional reflectance, Journal of Geophysical Research, 100, 21,077–21,089, https://doi.org/10.1029/95JD02371, 1995.

Wu, L., Hasekamp, O., van Diedenhoven, B., and Cairns, B.: Aerosol retrieval from multiangle, multispectral photopolarimetric measurements: importance of spectral range and angular resolution, Atmospheric Measurement Techniques, 8, 2625–2638, https://doi.org/10.5194/amt-8-2625-2015, 2015.

Wu, L., Hasekamp, O., Hu, H., aan de Brugh, J., Landgraf, J., Butz, A., and Aben, I.: Full-physics carbon dioxide retrievals from the Orbiting Carbon Observatory-2 (OCO-2) satellite by only using the 2.06 μm band, Atmospheric Measurement Techniques, 12, 6049–6058, https://doi.org/10.5194/amt-12-6049-2019, 2019.

Wu, L., aan de Brugh, J., Meijer, Y., Sierk, B., Hasekamp, O., Butz, A., and Landgraf, J.: XCO_2 observations using satellite measurements
710   with moderate spectral resolution: investigation using GOSAT and OCO-2 measurements, Atmospheric Measurement Techniques, 13,
    713–729, https://doi.org/10.5194/amt-13-713-2020, 2020.

Wunch, D., Wennberg, P. O., Toon, G. C., Connor, B. J., Fisher, B., Osterman, G. B., Frankenberg, C., Mand rake, L., O'Dell, C., Ahonen, P.,
    Biraud, S. C., Castano, R., Cressie, N., Crisp, D., Deutscher, N. M., Eldering, A., Fisher, M. L., Griffith, D. W. T., Gunson, M., Heikkinen,
    P., Keppel-Aleks, G., Kyrö, E., Lindenmaier, R., Macatangay, R., Mendonca, J., Messerschmidt, J., Miller, C. E., Morino, I., Notholt, J.,
715   Oyafuso, F. A., Rettinger, M., Robinson, J., Roehl, C. M., Salawitch, R. J., Sherlock, V., Strong, K., Sussmann, R., Tanaka, T., Thompson,
    D. R., Uchino, O., Warneke, T., and Wofsy, S. C.: A method for evaluating bias in global measurements of CO_2 total columns from space,
    Atmospheric Chemistry & Physics, 11, 12 317–12 337, https://doi.org/10.5194/acp-11-12317-2011, 2011.

Xu, F., van Harten, G., Diner, D. J., Kalashnikova, O. V., Seidel, F. C., Bruegge, C. J., and Dubovik, O.: Coupled retrieval of aerosol properties
    and land surface reflection using the Airborne Multiangle SpectroPolarimetric Imager, Journal of Geophysical Research (Atmospheres),
720   122, 7004–7026, https://doi.org/10.1002/2017JD026776, 2017.